

# Long Term Variability of Cyg X-1

## IV. Spectral Evolution 1999–2004

J. Wilms<sup>1</sup>, M.A. Nowak<sup>2</sup>, K. Pottschmidt<sup>3</sup>, G.G. Pooley<sup>4</sup>, and S. Fritz<sup>5</sup>

<sup>1</sup> Department of Physics, University of Warwick, Coventry, CV7 1AL, UK

<sup>2</sup> MIT-CXC, NE80-6077, 77 Massachusetts Ave., Cambridge, MA 02139, USA

<sup>3</sup> Center for Astrophysics and Space Sciences, University of California at San Diego, La Jolla, CA 92093-0424, USA

<sup>4</sup> Mullard Radio Astronomy Observatory, Cavendish Laboratory, Madingley Road, Cambridge CB3 0HE, UK

<sup>5</sup> Institut für Astronomie und Astrophysik, Universität Tübingen, Sand 1, 72076 Tübingen, Germany

Received <date> / Accepted <date>

**Abstract.** Continuing the observational campaign initiated by our group, we present the long term spectral evolution of the Galactic black hole candidate Cygnus X-1 in the X-rays and at 15 GHz. We present ~200 pointed observations taken between early 1999 and late 2004 with the Rossi X-ray Timing Explorer and the Ryle radio telescope. The X-ray spectra are remarkably well described by a simple broken power law spectrum with an exponential cutoff. Physically motivated Comptonization models, e.g., by Titarchuk (1994, compTT) and by Coppi (1999, eqpair), can reproduce this simplicity; however, the success of the phenomenological broken power law models cautions against “overparameterizing” the more physical models. Broken power law models reveal a significant linear correlation between the photon index of the lower energy power law and the hardening of the power law at ~10 keV. This phenomenological soft/hard power law correlation is partly attributable to correlations of broad band continuum components, rather than being dominated by the weak hardness/reflection fraction correlation present in the Comptonization model. Specifically, the Comptonization models show that the bolometric flux of a soft excess (e.g., disk component) is strongly correlated with the compactness ratio of the Comptonizing medium, with  $L_{\text{disk}} \propto (\ell_h/\ell_s)^{-0.19}$ . Over the course of our campaign, Cyg X-1 transited several times into the soft state, and exhibited a large number of “failed state transitions”. The fraction of the time spent in such low radio emission/soft X-ray spectral states has increased from ~10% in 1996–2000 to ~34% since early 2000. We find that radio flares typically occur during state transitions and failed state transitions (at  $\ell_h/\ell_s \sim 3$ ), and that there is a strong correlation between the 10–50 keV X-ray flux and the radio luminosity of the source. We demonstrate that rather than there being distinctly separated states, in contrast to the timing properties the spectrum of Cyg X-1 shows variations between extremes of properties, with clear cut examples of spectra at every intermediate point in the observed spectral correlations.

**Key words.** stars: individual (Cyg X-1) – binaries: close – X-rays: binaries – black hole physics

### 1. Introduction

One of the major results of X-ray and  $\gamma$ -ray astronomy since the discovery of Galactic black hole candidates (BHCs) more than thirty years ago has been the realization of the complexity of the spectral variability of these sources on time scales from milliseconds to decades. It is generally believed that this variability can provide clues as to the basic physical processes in X-ray binaries. Importantly, the broad-band spectra and timing behavior of accreting stellar mass black holes in X-ray binaries and of supermassive black holes in the centers of Active Galactic Nuclei (AGN) are very similar (Uttley et al. 2002; Uttley et al. 2005). Due to the scaling of the dynamical time scales in these systems with the mass of the central object, studying Galactic and extragalactic systems is complementary. Galactic sources

allow us to see how the accretion process evolves on very long time scales, while AGN provide “snapshot” observations of the accretion process, over characteristic dynamical time scales, with a signal to noise ratio that is not reachable for Galactic sources.

Observations over the last three decades have shown that Galactic BHC exhibit distinct and very characteristic states with different spectral shape and variability behavior, with AGN seemingly following similar trends (McHardy et al. 2005; Jester 2005, and therein). The state of a BHC depends on not yet fully understood parameters (Homan et al. 2001), although it is believed that the mass accretion rate,  $\dot{M}$ , and therefore the luminosity of the accreting system, plays a vital role. See McClintock & Remillard (2003) and Belloni (2004) for an extensive discussion of these issues.

For low accretion luminosities in the “hard state” of Galactic black holes, the X-ray spectrum can be described by a hard power law with photon index  $\Gamma \sim 1.7$  and an exponential cutoff at  $\sim 150$  keV. At low energies, most BHC show some kind of soft excess with a characteristic temperature of a few 100 eV. This baseline continuum is modified by a Fe  $K\alpha$  emission line at  $\sim 6.4$  keV and by reflection features, indicating the close proximity of the source of hard X-rays and relatively cold material. The hard state is furthermore characterized by strong X-ray variability of  $>10\%$  rms and by the presence of radio emission. In systems where the radio sources have been resolved, this radio emission has been shown to originate in an outflow that is consistent with being mildly relativistic ( $v \sim 0.6c$ ) in the hard state (Stirling et al. 2001; Gallo et al. 2003). For Cyg X-1, this outflow has recently been shown to have a time averaged kinetic power of  $\sim 10^{36}$  erg s $^{-1}$  to  $10^{37}$  erg s $^{-1}$ , i.e., a significant fraction of the system’s X-ray luminosity (Gallo et al. 2005).

In contrast to the “hard state”, the (typically) higher luminosity “soft state” exhibits a soft X-ray spectrum that can be well described by thermal emission from a standard accretion disk. Where a hard spectral component is detected, it does not show any appreciable curvature, sometimes up to the MeV regime (Grove et al. 1998; McConnell et al. 2000, 2002). The X-ray variability during the soft state is weak ( $\lesssim 6\%$  rms) and no radio emission is detected (Fender et al. 1999).

While there is general agreement that the soft excess is due to emission from an accretion disk, the interpretation of the hard spectral component and its relationship to the reprocessing features is still debated. The canonical interpretation of the hard state X-ray spectrum, first proposed in the 1970s (e.g., Thorne & Price 1975; Shapiro et al. 1976; Sunyaev & Trümper 1979) and later elaborated upon, e.g., by Haardt & Maraschi (1991) and Haardt & Maraschi (1993), is that the hard spectral component is caused by Comptonization, where soft X-rays from the inner disk are Compton upscattered by hot electrons ( $kT_e \sim 100$  keV) in a predominantly thermal electron gas, often called the “accretion disk corona” (ADC). The spectrum emerging from the corona has the proper power law plus exponential cutoff shape. To explain the presence of the ADC, magnetohydrodynamical instabilities (e.g., Balbus & Hawley 1998, and references therein), which only work efficiently at lower  $\dot{M}$ , have been invoked.

Observations limit the covering factor of the ADC with respect to the source of soft X-rays to  $\ll 1$ . Otherwise the ADC would fail to reach the high coronal temperatures, inferred from the energy of the exponential cutoff, due to efficient Compton cooling (e.g., Haardt et al. 1997; Dove et al. 1997a,b, and therein). Geometric models invoked to achieve smaller ADC covering factors include patchy coronae (Stern et al. 1995), magnetic flares (Beloborodov 1999; Poutanen & Fabian 1999), advection dominated accretion flows (Esin et al. 1998), ADCs with non-static or outflowing coronae (Beloborodov & Illarionov 2001; Malzac et al. 2001), and accretion flows with an inner geometrically thick ADC and an outer geometrically thin and optically thick accretion disk (Dove et al. 1997a,b). In all of these models, a fraction of the hard X-rays is scattered back towards the disk, giv-

ing rise to fluorescence Fe  $K\alpha$  emission and the Compton reflection hump (Lightman & Rybicki 1979; Lightman & White 1988). Comparisons between observations and theoretical model spectra for all of these different geometries have been successful.

With the realization of the importance of jets and their association with the hard state, the “Comptonization paradigm” has recently been challenged. The discovery of a tight correlation between the radio and the X-ray emission on time scales of days (Hannikainen et al. 1998; Pooley et al. 1999; Corbel et al. 2000) suggests a close coupling between the X-ray and the radio emitting media (Markoff et al. 2003; Heinz & Sunyaev 2003). In addition, in a direct comparison between data and theory, jet models capable of reproducing the radio–X-ray correlations have been recently shown to describe the X-ray spectrum with a precision comparable to Comptonization models (Markoff et al. 2005). The origin of the X-rays in these models is due to a combination of synchrotron emission from the jet and synchrotron self Compton emission from the jet base. We note, however, that a small separation of the emission regions cannot be ruled out from joint radio–X-ray timing arguments (Gleissner et al. 2004a), furthermore, accretion models postulating a strong coupling between a Comptonizing medium and the jet are also able to explain the radio–X-ray correlation without postulating a jet origin for the X-rays (Meier 2001; Merloni & Fabian 2002).

In conclusion, all existing models suggest a complex interplay between the energetics and emission from the accretion disk, Comptonizing plasma, and radio jet. This interplay can be disturbed by changes in some external parameter, such as  $\dot{M}$ . These changes may lead to state changes as well as to subtle changes in the overall source properties, such as the so called “failed state transitions” (Pottschmidt et al. 2000). An empirical understanding of the overall accretion process is therefore difficult to gain from only a few single and isolated observations, although these are very important for determining broad band spectra or for measuring spectra with high energy resolution (e.g., Miller et al. 2002). Monitoring campaigns covering the characteristic time scales of these spectral changes are required. We note that the necessity of monitoring campaigns follows also from hysteresis effects seen in many sources, i.e., the earlier source history is important for determining the source properties in a given observation (Miyamoto et al. 1995; Nowak et al. 2002; Maccarone & Coppi 2003).

Monitoring campaigns using large effective area and proportional counter energy resolution became possible in the 1990s with the *Rossi X-ray Timing Explorer* (RXTE). Since then, monitoring campaigns using RXTE’s pointed instruments, the Proportional Counter Array, (PCA; Jahoda et al. 1997) and the High Energy X-ray Timing Experiment, (HEXTE; Rothschild et al. 1998), have been performed for virtually all known persistent and transient Galactic black hole candidates. Among many others, examples for such campaigns are those on LMC X-1 and LMC X-3 (Nowak et al. 2001; Wilms et al. 2001), GX 339–4 (Wilms et al. 1999; Nowak et al. 1999, 2002; Kong et al. 2002; Homan et al. 2005; Belloni et al. 2005), V1408 Aql (Nowak & Wilms 1999), 4U 1543–47 (Kalemci et al. 2005), XTE J1650–500

(Kalemci et al. 2003), 4U 1630–47 (Tomsick & Kaaret 2000), and XTE J1550–564 (Kalemci et al. 2001; Sobczak et al. 2000).

In this paper, we present results from one of the longest of these monitoring campaigns, which was initiated by the authors in 1996 to be performed on the prototypical hard state black hole candidate (BHC) Cygnus X-1. Our campaign consists of biweekly,  $\sim 5$  ksec long *RXTE* pointings and simultaneous radio observations at 15 GHz ( $\lambda = 2$  cm) with the Mullard Radio Astronomy Observatory’s Ryle telescope in Cambridge, UK. Earlier papers in this series concentrated on the evolution of X-ray time lags (Pottschmidt et al. 2000), of the power spectrum (Pottschmidt et al. 2003b, hereafter paper i), the linear relationship between the short term root mean square variability and the flux (Gleissner et al. 2004b, hereafter paper ii), and correlations between the soft X-rays and the radio flux (Gleissner et al. 2004a, hereafter paper iii). Amongst others, archival data from the campaign have also been used in the discovery of giant flares from Cyg X-1 (Gierliński & Zdziarski 2003), a subset of the archival observations was also used in studies of Cyg X-1’s spectral and temporal variability (Axelsson et al. 2005; Ibragimov et al. 2005). Here, we discuss the results obtained on the spectral evolution of Cyg X-1 throughout the *RXTE* monitoring campaign, starting in Sect. 2 with a description of the changes of our data reduction procedure with respect to papers i through iii. In Sect. 3 we give the results of modeling the broad band 3–200 keV X-ray spectra using empirical spectral models as well as advanced Comptonization models and consider the evidence for interaction between the X-ray and the radio emission. We summarize our results in Sect. 4. We will discuss the joint spectral-timing behavior of Cyg X-1 based on our analyses in a future paper.

## 2. Data Reduction

### 2.1. Overview

We have already given an extensive overview of the *RXTE* observing strategy and our data extraction in papers i through iii. Here, we only highlight the most important points pertaining to the X-ray spectral analysis, mainly centered on the *RXTE* calibration.

In this paper we consider 202 observations with a typical good time of 3–7 ksec, for a total good time of  $\sim 989$  ksec. We use data from both the PCA and the HEXTE. Spectra are extracted with HEASOFT 5.3.1 and then fit with XSPEC 11.3.1w (Arnaud 1996). For the spectral analysis, we generated 3–25 keV PCA spectra from the top Xenon layer data and analyze spectra taken with different numbers of proportional counter units (PCUs) separately. This choice was made to allow the comparability with the results of the timing analysis. For the HEXTE, data from 18–120 keV were considered.

As shown in Appendix A, compared to earlier versions of the response matrices, the PCA is now in much better agreement with the HEXTE and also with other missions, in both, flux and spectral slope, with the remaining uncertainty being taken into account by a multiplicative constant that is normally very close to unity. Our reevaluation of the PCA cali-

bration also shows that remaining calibration uncertainties can be modeled to first order by adding a systematic uncertainty of 0.5% to the data, although even with this choice some significant calibration effects are still visible in the residuals (see Appendix A). As shown in Appendix B, however, this systematic error leads to a dramatic overestimation of the range of the confidence intervals for the fit parameters. Thus, although we compute confidence intervals at the 90% level for one interesting parameter, we do not show error bars in the figures.

The good time of the observations is mainly defined by excluding times of high PCA background. Due to the requirements of X-ray timing analysis, early in the campaign very conservative constraints were chosen, i.e., data taken within 30 minutes of passages through the South Atlantic Anomaly (SAA) and during times of high particle background were discarded. While in principle improved PCA background models now allow for good results even closer to the SAA passages, for consistency reasons and in order to facilitate the comparison of spectral parameters to the results of papers i through iii, the previous limits were retained.

Electronic tables in the Flexible Image Transport System (FITS) format containing the results of the spectral fitting and the confidence intervals for all best fit parameters are available accompanying the electronic version of this paper<sup>1</sup>. In our discussion of peculiar observations below, we identify observations in a way that makes it easy to find them in these FITS files and in the *RXTE* archive. The abbreviated syntax used is of the type Pxxxx/XX where xxxxx is the *RXTE* proposal ID and where XX is the number of the observation within each proposal. We also give the date and time of the observation to the closest hour and, in cases where an observation resulted in more than one spectrum because different detector combinations were used, we identify those detectors that were off.

### 2.2. Fitting Strategy

For larger data sets, the CPU time needed to perform spectral fitting can be considerable and therefore the choice of starting parameters for spectral modeling and how the spectral fits are performed is of some practical importance. We note that the most obvious strategy of spectral modeling, namely using the best fit values of nearby observations, can severely bias the correlations found between different spectral parameters as this strategy can force larger numbers of data points onto local  $\chi^2$ -minima. This bias is less of an issue when always using the same starting parameters, which is the approach adopted for the fits described below, even though this approach requires a larger amount of CPU time.

We also find that for complex models, such as the Comptonization fits described in Sect. 3.4 and 3.5, the  $\chi^2$ -valley exhibits a large number of local minima and there are many degeneracies between parameter combinations. Both effects result in a significant fraction of fits converging on local  $\chi^2$ -minima. Even when employing standard tricks, such as

<sup>1</sup> Tables 1–3 are only available in electronic form at the CDS via anonymous ftp to cdsarc.u-strasbg.fr (130.79.128.5) or via <http://cdsweb.u-strasbg.fr/cgi-bin/qcat?J/A+A/>

computing error contours, the global minimum was not always reached. These “rogue fits” can be identified through outliers in one or more parameters when looking at correlations between different spectral parameters. Where we identified such bad fits we refit the data using a different set of starting parameters obtained from “typical fits” using the same model.

A potential drawback of this approach is that it effectively forces these observations onto the correlations. Only about 20% of our observations, however, had to be treated in this labor intensive way. For a small fraction of these refitted observations, the  $\chi^2_{\text{red}}$  of the finally adopted spectral model was found to be *larger* by  $O(0.01)$  than the original  $\chi^2_{\text{red}}$  due to degeneracies between the fitting parameters. A typical example here are fits where the Fe  $K\alpha$  line energy pegs at its (unphysical) lower bound of 6 keV, which is often the case because of the PCA calibration uncertainty around the Xe L-edge. In such cases we searched for better models with the Fe line energy at  $\sim 6.4$  keV and accepted the best fit parameters from these fits, even if their  $\chi^2$  was slightly higher. The number of observations for which such a strategy was required is still small enough, and the increase of  $\chi^2$  was only  $O(0.01)$ , such that this strategy does not influence the results listed below and we are confident that all parameters shown in the following reflect the physical behavior of Cyg X-1.

In general, for all spectral fits presented here we find that for the reduced  $\chi^2$ ,  $\chi^2_{\text{red}} \lesssim 2$ . Values of  $\chi^2$  clearly larger than 1 might appear worrisome at first, however, we stress that the signal to noise ratio of our observations is very high and that the available spectral models are often too simple to be able to describe all subtleties of the observations. Furthermore, given our choice of systematics, for lower  $\chi^2_{\text{red}}$  PCA data are completely dominated by calibration uncertainties. In principle this would require data analysis methods that treat systematic errors in a much more elaborate way. We stress that typical observations of bright sources with other satellites, such as *Chandra* or *XMM-Newton*, result in good  $\chi^2$  values despite having significantly *larger* (10% or more) deviations between the data and the model than our *RXTE* fits, where we typically find that data and model deviate by  $<1\%$ . These better  $\chi^2$  values from *Chandra* and *XMM-Newton* are by virtue of their smaller effective areas and consequently larger Poisson errors which dominates over the calibration uncertainty of these satellites. Seen in this light, our *RXTE* models thus provide an overall good description of the spectral shape of Cygnus X-1.

### 3. Modeling the 3–200 keV Spectrum of Cygnus X-1

#### 3.1. Cygnus X-1 since the launch of RXTE

Fig. 1 shows the X-ray and radio lightcurves of Cyg X-1 for the nine year long interval from early 1996 (launch of *RXTE*) until the end of 2004. Shown are the 2–10 keV X-ray flux measured with the *RXTE* All Sky Monitor (Levine et al. 1996), as well as the radio lightcurves at 15 GHz from the Ryle telescope and at 2.25 GHz and 8.3 GHz measured with the Green Bank interferometer (GBI; these data are only available until early 2000 when the GBI monitoring campaign was discontinued due to lack of funding). To minimize the significant source variability

on its orbital time scale (Brocksopp et al. 1999a) and to emphasize the long-term evolution of the source, the data were rebinned to a resolution of 5.6 d.

The figure clearly shows the well known fact that Cyg X-1 transits between two states. As will be elaborated upon below, for ASM count rates below  $\sim 45$  cps, the source is in a classical hard state. During this time radio emission is observed at a level of  $\sim 12$  mJy at 15 GHz. In contrast, during times when the ASM count rate is  $\geq 80$  cps, the source spectrum is soft, although a hard power law component is still seen. We will call these phases the “soft state”, although it is important to note that Cyg X-1 only rarely reaches what one would call a classical “soft state” in transient BHC. During these soft states, the radio emission is strongly reduced. We especially note that during the long soft state of 2001/2002 there were phases where no radio emission could be detected (mm-emission was quenched during that time as well; Tigelaar et al. 2004).

During transitions between the hard and soft states, radio flares are observed where the radio flux can be up to a factor of two higher than during the hard state. Cyg X-1 also shows short episodes where the ASM count rate increases. We have identified these episodes with “failed state transitions” before (paper i), since they are characterized by the X-ray spectrum softening and by clearly changed timing properties (e.g., increased X-ray time lags Pottschmidt et al. 2000), similar to state transitions, although the source never really settles into a soft state like behavior.

Prior to  $\sim 1999$ , Cyg X-1 was in the hard state for most of the time, except for rather short “failed state transitions” and the short soft state of 1996. From that time onwards, the frequency of the failed state transitions increased until, from 2001 July onwards, Cyg X-1 reached the long 2001/2002 soft state. It stayed in this phase for almost a year until 2002 August/September where it rapidly transited back into the hard state, with a spectrum similar to before the soft state. Shortly after this, in 2003 June and at the turn of 2003/2004, two other short soft state episodes occurred. From early 2004 onwards, the *RXTE* ASM count rate was generally increased with respect to the 1997–1999 hard states and the source spectrum was generally softer as well.

We can quantify this behavior for the moment by defining the hard state to have an orbit averaged ASM count rate of  $<45$  cps (see Sect. 3.3) and the soft state to have an ASM count rate  $\geq 80$  cps. Using these definitions, for the total time interval from 1996–2004, Cyg X-1 spent 75% of the time in the hard state, 4% in the soft state and 21% in between. Before MJD 51300, the source was in the hard state for 90% of the time, in the soft state 4% of the time, and in between for  $\sim 6\%$  of the time. These numbers change dramatically after MJD 51300, where the time spent in the hard state decreased to 66%, while the soft and intermediate phases account for 34% of all ASM data points. While these numbers are not too precise because of our arbitrary cuts between the different states in terms of the ASM count rate, they clearly point towards a change in source behavior in recent years, which might have been foreshadowed by a change in the timing properties of the source around MJD 50920 (see Fig. 3 of paper i). Specifically, around this time the short time scale rms variability (i.e., the rms as-

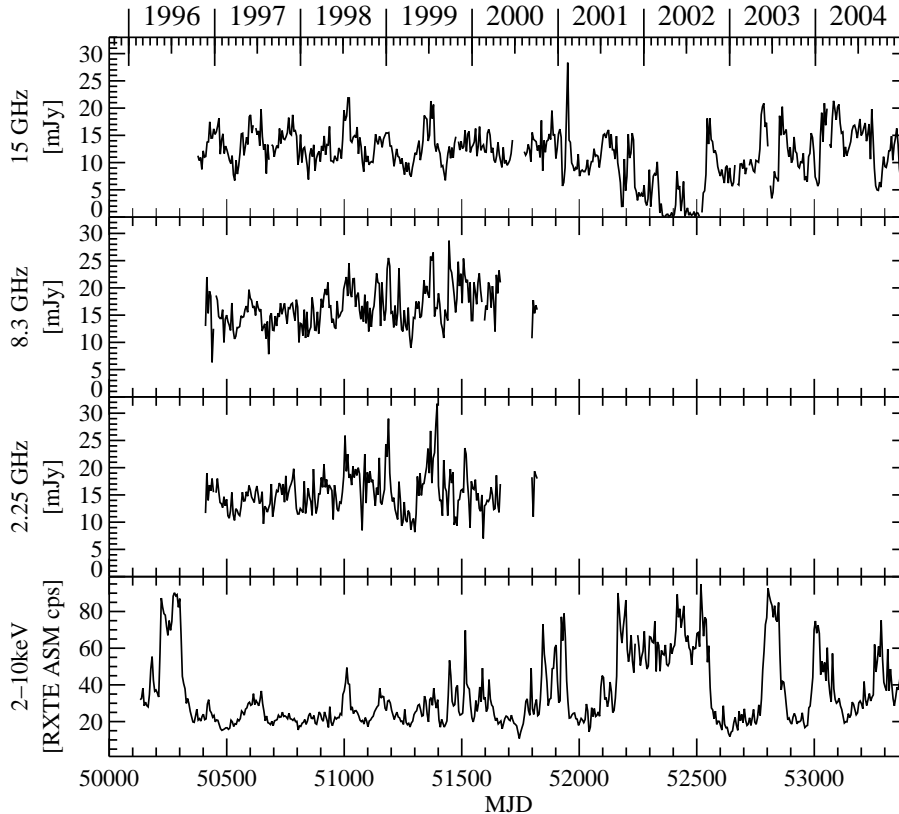


**Fig. 1.** *RXTE*-ASM 2–10 keV, and radio lightcurves of Cyg X-1 from 1996 until the end of 2004. The 15 GHz data are from the Ryle telescope, the 8.3 GHz and 2.25 GHz measurements come from the National Radio Astronomy Observatory’s Green Bank Interferometer. The data are rebinned to a resolution of 5.6 d to smooth out the orbital variability.

sociated with individual pointed observations) significantly decreased, while the long time scale variability (i.e., the prevalence of failed state transitions) increased.

The physical reason for this change of behavior after  $\sim$ MJD 51000 is unclear. In its simplest interpretation, the soft state occurs at higher  $\dot{M}$ , and thus one could speculate that the mass accretion rate increased around that date. As  $\dot{M}$  is related to the mass loss rate of HDE 226868, in principle it is possible to measure  $\dot{M}$  from its correlation with the equivalent width (EW) of the  $H\alpha$  line (Puls et al. 1996). The simplest picture, that a higher mass loss rate of HDE 226868 results in a higher  $\dot{M}$  for the black hole, however, is contradicted by the observations. Contrary to expectations, the soft state  $H\alpha$  EW is generally lower than in the hard state (Voloshina et al. 1997; Brocksopp et al. 1999a; Gies et al. 2003; Tarasov et al. 2003). For single stars, such a behavior indicates a *lower* mass loss rate (Gies et al. 2003, and therein). A possible solution to this enigma is that photoionization by the X-ray source changes the wind ionization state (Hatchett & McCray 1977). Observationally, this effect could be the cause of the variation of the  $H\alpha$  line profile with orbital phase (Gies et al. 2003; Tarasov et al. 2003). To explain the relation between the X-rays and the optical data, both teams of authors suggest that a decrease in the mass loss rate of HDE 226868,  $\dot{M}_w$ , changes the properties of the accretion flow onto the black hole. A decreased wind density results in an increase of the size of the Strömgren sphere around the X-ray source, resulting in a lower radiative acceleration and consequential lower terminal wind velocity,  $v_w$ . Since the mass accretion rate is  $\dot{M} \propto \dot{M}_w/v_w^4$  (Bondi & Hoyle 1944; Davidson & Ostriker 1973), an increase

of  $\dot{M}$  through the accretion disk is triggered, leading to the increase in soft X-ray emission. The sparse optical coverage prohibits so far direct tests whether this picture is true, although at least for one failed state transition, Tarasov et al. (2003) find a decrease of the EW before the flare, consistent with the above model. If this general idea is correct, it then follows that the recent increase in soft state activity of Cyg X-1 could be linked to episodes of lower mass loss from HDE 226868 (Gies et al. 2003), e.g., linked to activity cycles of the donor star.

### 3.2. Choice of Spectral Models

A major issue with describing Galactic black hole X-ray spectra is the choice of the models to be employed; a multitude of more or less physically motivated models are available. It is often found that several of these models describe the X-ray data equally well in a  $\chi^2$  sense (Nowak et al. 2002). Unfortunately, however, it can be difficult to directly compare spectral parameters obtained from these physically motivated models, as they often make different implicit assumptions in their physical setup (Nowak et al. 2002; Coppi 2004, and references therein). For example, Comptonization models differ in their assumptions on the spectral shape of the seed photons (e.g., Wien spectrum versus black body versus accretion disk spectrum) and they also assume different geometries for the source of the seed photons and of the Comptonizing medium (Nowak et al. 2002; Coppi 2004). These assumptions greatly complicate a direct comparison even of “simple” parameters such as the covering factor of the reflecting medium.

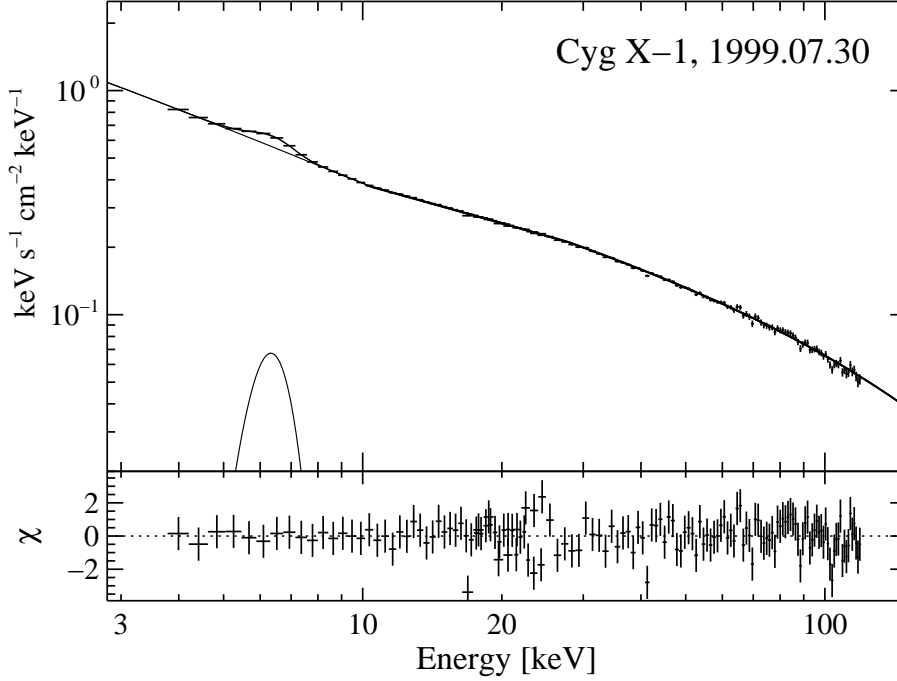


**Fig. 2.** Unfolded spectrum and residuals for the Cyg X-1 observation of 1999 July 30 (P40090/14), using the broken power law model as the baseline continuum.

Here, we use an approach already used by us earlier in a study of GX 339–4 (Nowak et al. 2002) to describe the spectral evolution of Cyg X-1 using several different spectral models. We start in Sect. 3.3 with the most simple spectral model, a broken power law with an exponential cutoff. This model gives a very good empirical description of the hard state X-ray spectral shape. We then use two different physically motivated models to find an interpretation of the empirically derived spectral shape in terms of Comptonization. In Sect. 3.4 we use the widely available Comptonization model of Titarchuk (1994, see also Titarchuk & Lyubarskij 1995; Titarchuk & Hua 1995), *compTT*. We contrast the *compTT* results in Sect. 3.5 with the more elaborate Comptonization model *eqpair* (Coppi 1992, 1999), which provides a good example for today's class of self-consistent Comptonization models that also include the capability to generate the spectra resulting from non-thermal Comptonization.

### 3.3. Empirical models: Broken Power Law Fits

To describe the spectrum of Cyg X-1 on purely empirical grounds, as originally motivated by our modeling of the broad band radio to X-ray spectrum of GX 339–4 and Cyg X-1, (Nowak et al. 2005), we model the joint PCA/HEXTE data with an absorbed broken power law with break energy  $E_{\text{break}}$ , soft photon index  $\Gamma_1$ , and hard photon index  $\Gamma_2$ , that is exponentially cutoff above an energy  $E_{\text{cut}}$  with an  $e$ -folding energy of  $E_{\text{fold}}$ . In addition to this continuum, all fits require an Fe  $K\alpha$  line at  $\sim 6.4$  keV, which we model as a Gaussian with energy  $E_{\text{Fe } K\alpha}$  and width  $\sigma_{\text{Fe } K\alpha}$ . Table 1, available in electronic form only (see footnote 1), contains all of these best fit parameters and their 90% confidence intervals, including  $\Gamma_1$ ,  $\Gamma_2$ ,  $E_{\text{fold}}$ ,  $E_{\text{break}}$ , and the Fe line parameters. The table also includes photon and energy fluxes determined from the model for the 2–5 keV, 5–10 keV, 10–50 keV, 50–100 keV bands and the un-

absorbed 2–100 keV flux. Furthermore, the table includes the time of each observation, its exposure time, and the PCA and HEXTE count rates.

Fig. 2 shows a typical example for a broken power law fit, illustrating that for most observations this continuum model gives a good description of the data, with  $\chi^2_{\text{red}} < 2$ . A similar result for broken power law fits has been found previously, e.g., by Gierliński et al. (1999). In general, we find that during the hard state the goodness of the broken power law fits as measured in terms of their  $\chi^2_{\text{red}}$  surpasses that of the *compTT* and *eqpair* fits. During the soft state, the broken power law fits still provide a very good description of the hard spectrum above  $\gtrsim 6$  keV, but fare less well below  $\sim 6$  keV where the accretion disk becomes important<sup>2</sup>. For these data, *compTT* and *eqpair* give a better description of the spectrum.

As shown in Fig. 3a, for all observations of Cyg X-1 studied here,  $\Gamma_2 < \Gamma_1$ , that is, the higher energy power law is spec-

<sup>2</sup> This failure of the simple broken power law is most evident for observations P50110/53 (2002.05.06:00), P60090/05 (2002.05.06:02), P60090/07 (2002.05.31:23) and P60090/15 (2002.09.20:16). These data are characterized by  $\Gamma_1 \gtrsim 3$ , i.e., they are amongst the softest in our sample and there is a clear thermal component present. As our main interest in this section is on the behavior of the harder spectrum, we ignored the data below 5 keV for these two observations. Above that energy, the spectrum could again be well described by a broken power law. Additionally, there are two peculiar observations, P50110/07 (2000.06.02:05) and P50110/10 (2000.07.15:00). In these observations,  $\Gamma_1 \sim \Gamma_2$  (but not equal!) and when both power law indices and the Fe line parameters are left free, the uncertainties of both power law indices are very large, the break energy in these observations converges to  $\sim 5.5$  keV and the energy of the Gaussian is found close to 5.5 keV with a width in excess of 1 keV, effectively smoothing out the effect of the break. Rather than forcing the power law indices to some (arbitrary) value, we have decided to omit these two observations from the following analysis, although they are contained in Table 1.

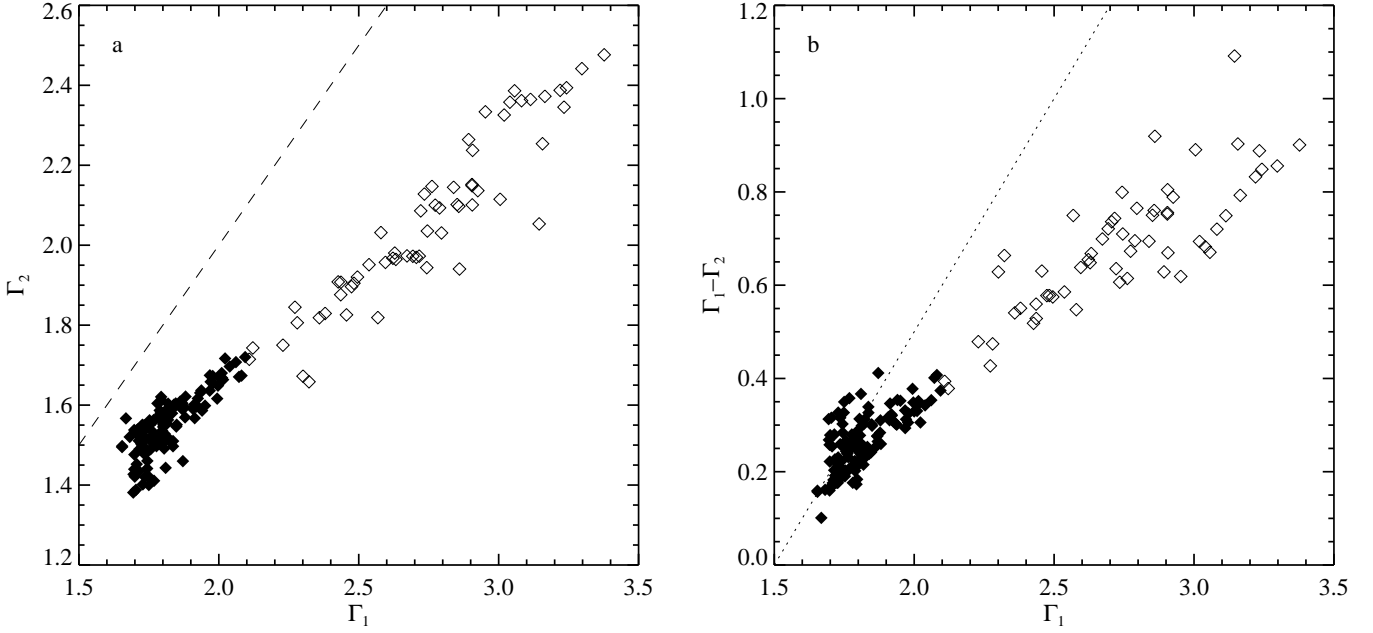


**Fig. 3. a)** Correlation between the soft power law index,  $\Gamma_1$ , and the hard power law index,  $\Gamma_2$ , for the broken power law fits. The dashed line corresponds to  $\Gamma_1 = \Gamma_2$ . Filled diamonds designate hard state observations, defined by  $\Gamma_1 \leq 2.1$ , open diamonds are intermediate and soft state observations. **b)** Correlation between soft energy power law index,  $\Gamma_1$ , and power law break,  $\Gamma_1 - \Gamma_2$ , for the broken power law fits. Lines parallel to the dotted line correspond to lines of constant  $\Gamma_2$ . For both correlations, Spearman's rank correlation coefficient  $\rho = 0.916$ .

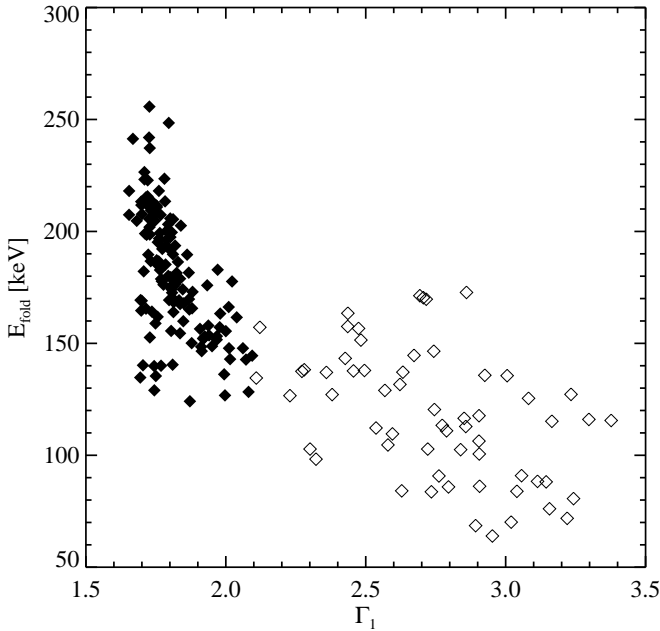


**Fig. 4.** Correlation between the photon index of the soft power law index,  $\Gamma_1$ , and the  $e$ -folding energy of the hard continuum,  $E_{\text{fold}}$ , for the broken power law fits. Symbols are the same as in Fig. 3

trally harder than the soft one. For the majority of our fits, the break energy of the power laws is found between 15 and 40 keV. There is a weak correlation between  $E_{\text{break}}$  and  $E_{\text{fold}}$

in the sense that higher break energies also have higher folding energies. A similar correlation exists between  $\Gamma_1$  and  $E_{\text{fold}}$  (Fig. 4), where we find that a softer continuum implies more curvature at high energies than harder spectra. In Fig. 3 and all following figures showing spectral parameters, we show data points from the hard state with the filled symbols and data from observations from the intermediate and soft state using open symbols. To define the hard state, we use  $\Gamma_1 < 2.1$  (a simplified version of the classification of Remillard 2005), corresponding to ASM count rates below  $45 \text{ counts s}^{-1}$ .

The most interesting property of the broken power law fits is the hardening of the broken power law, which can be physically interpreted as the hardening of the underlying continuum caused by Compton reflection off cold or mildly ionized material. As has been pointed out by Zdziarski et al. (1999), for Seyfert galaxies and galactic black hole binaries, there is a correlation between the power law index and the covering factor of the reflecting medium,  $\Omega/2\pi$ , in the sense that softer power laws tend to show stronger reflection. Our broken power law fits show a similar correlation: There is a strong linear relationship between  $\Gamma_1$  and  $\Gamma_2$  (Fig. 3a). Correlating the soft power law index,  $\Gamma_1$  with the hardening of the broken power law at the break energy,  $\Delta\Gamma = \Gamma_1 - \Gamma_2$ , results in a similarly tight correlation (Fig. 3b). As discussed, e.g., by Zdziarski et al. (1999, and references therein), for standard power law plus reflection fits,  $\Gamma$  and  $\Omega/2\pi$  are not strictly independent fit parameters: During  $\chi^2$  minimization, softer power law continua can be compensated to some extent by increasing  $\Omega/2\pi$ . This behavior can lead to artificial correlations between these two parameters. While the range of  $\Omega$  and  $\Gamma$  used to derive the observed  $\Omega$ –

$\Gamma$  correlation was much larger than the systematic uncertainty caused by the non-independent fit parameters (Zdziarski et al. 1999), for sources where  $\Omega$  and  $\Gamma$  do not vary as much, the artificial correlation is still of some concern. In contrast, in the broken power-law fits  $\Gamma_1$  and  $\Gamma_2$  are virtually independent and therefore artificial correlations are not an issue for our analysis.

Lastly, we comment on the behavior of the Fe  $K\alpha$  line in the broken power law fits. In general, we find the line at 6.4 keV, i.e., consistent with neutral iron, although spectra showing a larger  $\Delta\Gamma$  tend to show slightly higher line energies. In no case does the line energy exceed 6.7 keV. This trend could indicate a slightly higher degree of disk ionization for the softer spectra during these episodes. The distribution of the line width,  $\sigma_{\text{Fe } K\alpha}$ , from all observations can be well described by a Gaussian distribution with a mean of 0.6 keV, consistent, e.g., with earlier *BeppoSAX* and *RXTE* results (Frontera et al. 2001; Gilfanov et al. 1999). We performed Monte Carlo simulations, confirming our experience that with its 18% FWHM energy resolution at 5.9 keV the PCA can resolve lines down to  $\sigma \sim 0.3$  keV. The fits indicate, therefore, that the Fe  $K\alpha$  line is slightly broadened, as has been found also with higher resolution instruments (e.g., Miller et al. 2002). Note, however, that the  $\sim 5$  keV calibration feature discussed in Appendix A as well as the presence of a soft excess can bias the line parameters towards a lower energy and larger  $\sigma$ .

### 3.4. Simple Comptonization Models: *compTT*

We now turn to modeling the data with more physically motivated spectral models. We first use the Comptonization model *compTT* (Titarchuk 1994; Titarchuk & Lyubarskij 1995; Titarchuk & Hua 1995), as historically it has met with good success in describing black hole spectra. Model parameters discussed here, therefore, can be used in comparisons with earlier results and other sources (see, e.g., Pottschmidt et al. 2003a). Furthermore, as we shall see below, the behavior of *compTT* parameters is very similar to that of the more sophisticated Comptonization models, while being substantially faster to fit.

We took *compTT* as the baseline continuum, assuming a disk geometry. The parameters of the continuum are the electron optical depth,  $\tau_e$ , and the electron temperature  $kT_e$ . An accretion disk continuum with a  $r^{-3/4}$  temperature profile and inner disk temperature  $kT_{\text{in}}$  (XSPEC model *diskbb*; Mitsuda et al. 1984; Makishima et al. 1986) was added to model the soft emission. We set the temperature of the seed photons for Comptonization equal to  $kT_{\text{in}}$ , indicating that the disk is the source of the seed photons. Note that this approach is only approximately justified, since the seed photon distribution assumed by *compTT* is a Wien distribution and not a proper disk spectrum. We take Compton reflection of the Comptonization continuum into account using the Green's functions of Magdziarz & Zdziarski (1995, XSPEC model *reflect*), assuming solar abundances, a neutral reflector, an inclination of  $40^\circ$ , and taking into account absorption in the interstellar medium and the stellar wind. The behavior of the latter is similar to that seen in the *eqpair* fits, so we will defer a discussion of the behavior of the Hydrogen equivalent

column,  $N_{\text{H}}$ , to Sect. 3.5. All best fit parameters, including  $kT_{\text{in}}$ ,  $\tau$ ,  $kT_e$ ,  $\Omega/2\pi$ , the Fe line parameters, and the model normalizations, as well as their 90% confidence intervals are available in the electronic Table 2 (see footnote 1). The table also includes fluxes from the model in the same standard bands as Table 1, as well as the total bolometric flux inferred from the model. Finally, the table also includes the total bolometric accretion disk flux.

The Fe  $K\alpha$  line was again modeled by a Gaussian, but with the Fe  $K\alpha$  line energy fixed at 6.4 keV (fits with the line energy free were virtually identical). There is one clear difference between the Fe  $K\alpha$  parameters in the broken power law fits and the ones found with *compTT*: Fe  $K\alpha$  line widths are greater by a factor of  $\sim 1.55$  than in the broken power law fits. Inspection of the *compTT* residuals shows the PCA to have a wavy structure at low energies around the Fe line, indicating that our choice of soft spectral components does not adequately describe the details of the shape of the soft continuum. In addition, we see the  $K\alpha$  line width increasing almost linearly with the accretion disk flux, until it saturates at  $F_{\text{disk}} \sim 10^{-8} \text{ erg cm}^{-2} \text{ s}^{-1}$  with a line width of  $\sim 1$  keV. Such a behavior is similar to that of a similarly broad line feature (at  $\sim 5.7$  keV) seen in XTE J1908+094, in the early and late phases of the outburst of this soft X-ray transient (Gögüş et al. 2004). The broader Fe  $K\alpha$  line width can thus be seen as an attempt of the  $\chi^2$ -minimization procedure to smooth out the continuum to provide a more power-law like soft continuum. This conclusion is verified by the generally worse  $\chi^2$  of the *compTT* fits compared to the broken power law ones, although in general the model is still providing a good description of the data: For hard state and intermediate state observations,  $\chi^2_{\text{red}} \lesssim 1.3$ , for soft state observations,  $\chi^2_{\text{red}}$  is clearly higher, although (except for four cases) still better than 2. Note that only in 12 out of the 202 observations is the  $\chi^2_{\text{red}}$  of the *compTT* fits better than that of the broken power law fits.

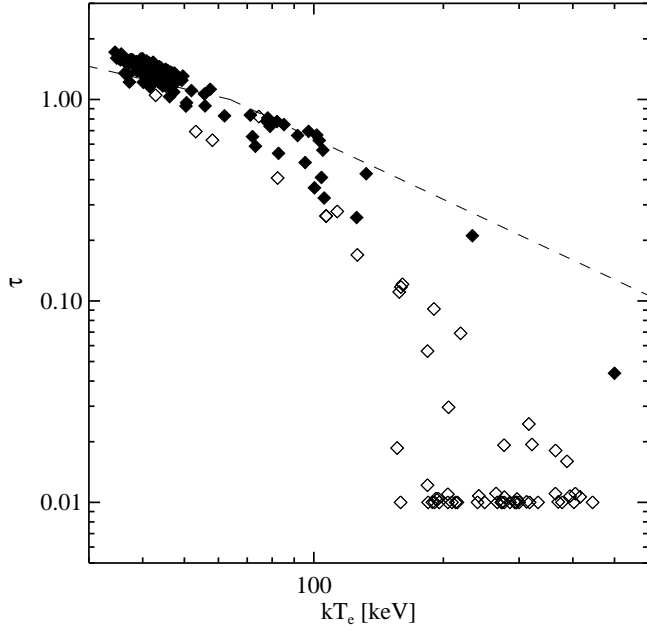
Replacing the disk component with a relativistic disk spectrum (XSPEC model *diskp*, Gierliński et al. 1999) resulted in significantly worse fits. Adding a second soft component (modeled either by a second disk spectrum or by optically thick Comptonization Gierliński et al. 1999) to our baseline *diskbb* model did not result in improving the residuals significantly either. We therefore decided to stick with our baseline model, especially since the Comptonization parameters are mainly driven by the harder spectrum.

Fig. 5 shows the correlation between the optical depth,  $\tau$ , and the temperature  $kT_e$  of the Comptonizing plasma. Defining the Compton  $y$  parameter in the usual fashion,

$$y = \frac{4kT_e}{m_e c^2} \max(\tau, \tau^2) \quad (1)$$

we find that for a large fraction of the data ( $\sim 70\%$  of the observations),  $y \simeq 0.5$  (Fig. 5, dashed line). That is, during these times the Compton- $y$  of the Comptonizing plasma is nearly constant to within our error bars. This behavior is a well known property of plasmas held in thermal equilibrium by balancing the available heating by Compton cooling (e.g., Dove et al. 1997a,b). Note that we set the lower limit of  $\tau$  to 0.01 in our fits. For  $\tau \lesssim 0.1$ , if  $y$  were to remain constant at such low optical depths, the plasma would have





**Fig. 5.** Correlation between the electron temperature of the Comptonizing plasma,  $kT_e$  and its optical depth,  $\tau$ . The dashed line shows the values for which the Compton  $y$  parameter  $y = 0.5$ , the lower limit for  $\tau$  set in the fits was  $\tau = 0.01$ . Symbols used are identical to Fig. 3.

relativistic temperatures, violating the approximations used in the `compTT` model (Titarchuk & Hua 1995). Processes such as photon-photon pair production would become important. For these conditions, more realistic Comptonization models such as `eqpair` have to be used (Sect. 3.5). We still find that  $y$  is well determined for these observations, with observations with  $kT_e \gtrsim 100$  keV leaving the track of constant  $y$  inferred above as  $\tau$  pegs at its lower limit. Virtually all of these observations were made during soft state episodes and are therefore characterized by a strong soft excess and a softer hard spectrum than the average hard state spectrum: The majority of spectra with a hard power law index of  $\Gamma_2 > 1.8$  in the broken power law fits come from observations for which the `compTT` fits yield  $kT_e > 100$  keV. This result is consistent with earlier studies of the 1996 soft state of Cygnus X-1 (e.g., Cui et al. 1997).

Since the parameter responsible for the shape of the Comptonization spectrum is the Compton- $y$ , we now study the relationship between the accretion disk and the reflection parameters and  $y$  (Figs. 6 and 7). In general, the correlations found in this way are much tighter than correlations with respect to  $kT_e$  and  $\tau$ , as these two parameters are strongly coupled.

We compute the bolometric unabsorbed flux of the accretion disk,  $F_{\text{disk}}$ , by integrating the `diskbb` component of the best fit model from 1 eV to 50 keV. The second source of soft photons, the Wien seed photon spectrum, is not taken into account. Comparison with the soft fluxes derived with `eqpair`, where the seed photons can be taken into account (see Sect. 3.5 below), shows that not taking the Wien spectrum into account results in the bolometric disk fluxes from `compTT` to be 73% of

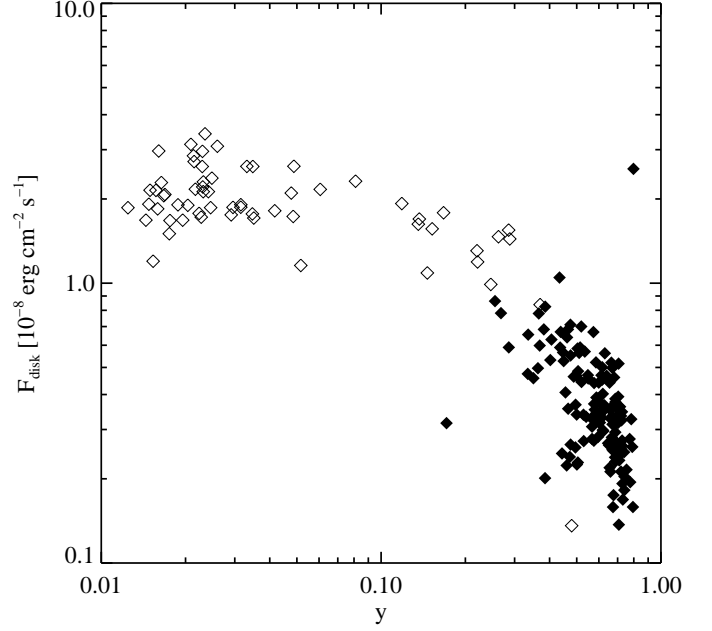


**Fig. 6.** Relationship between Compton- $y$  and the unabsorbed accretion disk flux for the `compTT` fits. Symbols used are the same as in Fig. 3.

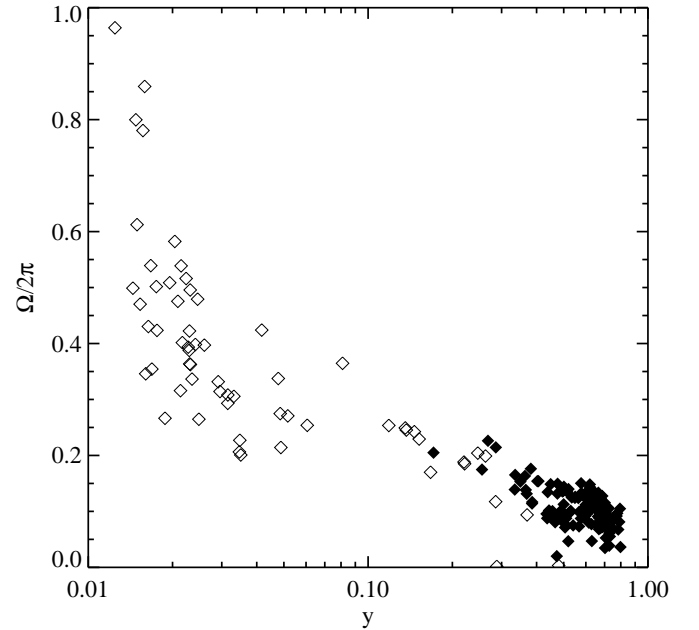


**Fig. 7.** Correlation between  $y$  and the covering factor for reflection,  $\Omega/2\pi$  for the `compTT` fits, showing that  $\Omega$  strongly increases for small  $y$ . Symbols used are the same as in Fig. 3.

the `eqpair` fluxes. After correcting the `compTT` fluxes for this offset, the standard deviation of the the `eqpair` and `compTT` ratio is found to 20%, which we take as the systematic uncertainty of the individual fluxes caused by extrapolating the best fit model outside of the energy range used for fitting. This 20% systematic uncertainty of individual flux points is much smaller

than the overall variation of the disk fluxes found in the data. Note that in the following, when quoting  $F_{\text{disk}}$  from `compTT` fits we do *not* apply any correction factor, such as might be caused by ignoring the Wien seed spectrum.

Fig. 6 shows how  $F_{\text{disk}}$  depends on  $y$ . There are clearly two regimes of different spectral behavior recognizable: During the hard state (filled symbols),  $F_{\text{disk}}$  is seen to vary by almost an order of magnitude, while  $y$  remains constant. At the same time,  $\Omega/2\pi$  varies only slightly (Fig. 7). This behavior of parameters holds for disk fluxes below  $\sim 10^{-8} \text{ erg cm}^{-2} \text{ s}^{-1}$ , corresponding to a threshold disk luminosity of  $4.8 \times 10^{36} \text{ erg s}^{-2}$  (assuming a distance of 2 kpc, see Ziolkowski 2005, and references therein). Above this threshold the intermediate or the soft state is reached. Here,  $y$  is seen to vary strongly, the disk luminosity is far less variable than before, and  $\Omega/2\pi$  varies strongly.

### 3.5. Comptonization: *eqpair*

We turn to the most sophisticated of the spectral models discussed here, the *eqpair* model (Coppi 1992, 1999). It is a hybrid thermal/nonthermal Comptonization code, and it includes electron-positron pair production. Given the overall success of thermal Comptonization to describe the hard X-ray spectrum described in Sect. 3.4, in the following we assume a fully thermal electron distribution. *Eqpair* computes the temperature of the Comptonizing medium self-consistently, by balancing external heating with Compton cooling of a defined seed-photon distribution, which in our case is the *diskpn* model (Gierliński et al. 1999). The amount of heating of the Comptonizing medium is specified in *eqpair* through the ratio of the compactnesses of the Comptonizing medium and the seed photon distribution,  $\ell_h/\ell_s$ , where the dimensionless compactness parameter of a medium of characteristic size  $r$  is defined by

$$\ell = \frac{L\sigma_T}{rm_e c^3} \quad (2)$$

where  $L$  is the source luminosity,  $\sigma_T$  the Thomson cross section,  $m_e$  the electron mass, and  $c$  the speed of light. To force the seed photon spectrum to be dominated by disk radiation, we fix  $\ell_s = 10$ . A fraction of the hard X-rays is scattered back onto the disk where it is reflected. The amount of reflection is again quantified by the covering factor for reflection,  $\Omega/2\pi$ , contrary to the `compTT` fits, relativistic smearing is taken into account for the reflection component.

Similar to the `compTT` fits, we model the soft excess by adding a *diskbb* to the continuum. In contrast, detectors with a lower energy threshold than the PCA often have shown the soft X-ray spectrum in *eqpair* modeling to be more complex than what we use here. The soft excess has been described by optically thick Comptonization of 100–300 eV disk photons (Bałucińska-Church et al. 1995), as predicted for the inner regions of Shakura & Sunyaev (1973) disks (Gierliński et al. 1997; Frontera et al. 2001; Di Salvo et al. 2001). Our spectra have an  $\sim 3 \text{ keV}$  lower threshold, thus we cannot describe in detail this component. Similar to the `compTT` fits, we find that adding a *diskbb* spectrum to the *eqpair* continuum results in a satisfactory description of the data. We set the inner

disk temperature to the maximum temperature of the *eqpair* seed photon distribution. Modeling the soft excess with the *diskbb* works better than with the *diskpn*, as the shape of the *diskbb* model better approximates the shape of a (saturated) Comptonization spectrum.

Absorption in the interstellar medium and in the stellar wind is taken into account using the model of Bałucińska-Church & McCammon (1992), letting the hydrogen equivalent column vary freely. We find a dependence of  $N_H$  with orbital phase (using the ephemeris of Brocksopp et al. 1999b), with  $N_H$  being higher by a factor  $\sim 2$  during superior conjunction, pointing towards significant absorption in the stellar wind of HDE 226868 (see Wen et al. 1999 for a similar conclusion based on *RXTE*-ASM data). We also confirm earlier results by Bałucińska-Church et al. (2000) of a secondary maximum of  $N_H$  around orbital phase 0.6, which earlier has been identified with absorption in the accretion stream. No other fit parameters show a significant dependence on orbital phase.

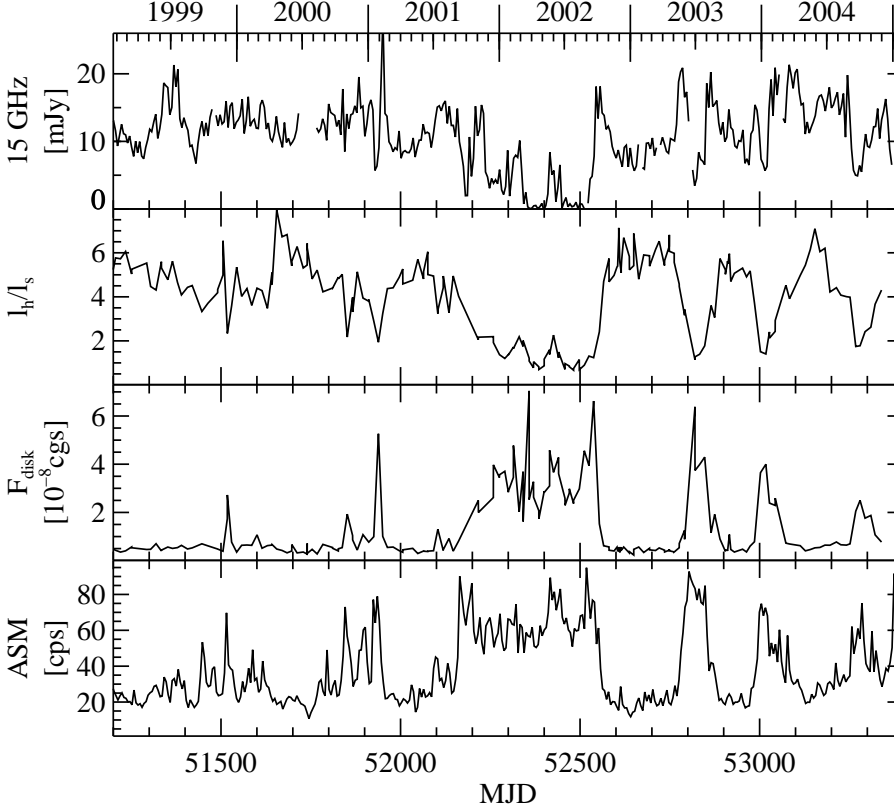
Using this approach, our fits gave  $\chi^2_{\text{red}}$  values similar to the models discussed in Sects. 3.3 and 3.4, with only a very weak dependence of  $\chi^2_{\text{red}}$  on the source state (softer spectra tend to have slightly worse  $\chi^2_{\text{red}}$ ). During the hard state,  $\chi^2_{\text{red}}$  for the *eqpair* fits is generally worse than that of the broken power law fits, while it is better during the soft state (we attribute the latter to us not including a thermal component in the broken power law fits). All best-fit parameters, including  $\ell_h/\ell_s$ ,  $\Omega/2\pi$ , and the Fe line parameters, and X-ray fluxes for the same bands as for the broken powerlaw and `compTT` fits, as well as unabsorbed fluxes for the accretion disk and for the broadband spectrum are contained in Table 3, which is available in electronic form only (see footnote 1).

Fig. 8 shows the evolution of energetics of the soft and the hard spectral components. Similar to the `compTT` fits, we characterize the soft flux by the unabsorbed bolometric accretion disk flux,  $F_{\text{disk}}$ . This flux is computed as the sum of the 1 eV–50 keV fluxes of the *diskpn*<sup>3</sup> and *diskbb* spectral components of the best fit models. As discussed in Sect. 3.4, the systematic uncertainty of these fluxes is estimated to be 20%, much smaller than the variations observed. Not unexpectedly, the disk flux is correlated with the binary orbit averaged *RXTE*-ASM count rate. A more careful analysis of the lightcurve reveals, however, that there the ASM does not always fully track  $F_{\text{disk}}$ . For example,  $F_{\text{disk}}$  increases significantly during the second and third of the three dominant soft flares around MJD 51500 and remains weak during the first. We will revisit these differences, which might be due to hysteresis effects similar to BHC transient outbursts, below. Overall, however, the correlation between  $F_{\text{disk}}$  and the ASM count rate is good, with the Spearman rank correlation coefficient indicating a highly significant correlation ( $\rho = 0.851$ ). A linear regression gives

$$\frac{F_{\text{disk}}}{10^{-8} \text{ erg cm}^{-2} \text{ s}} = 0.0592 \frac{F_{\text{ASM}}}{\text{counts s}^{-1}} - 0.809 \quad (3)$$

where  $F_{\text{ASM}}$  is the rebinned ASM count rate. Due to the hysteresis effects mentioned above, we estimate the uncertainty of

<sup>3</sup> The *eqpair* model has a toggle that allows one to calculate the flux of solely the seed photon component



**Fig. 8.** Spectral evolution of Cyg X-1 from 1999 until the end of 2004. Shown from top to bottom are the radio flux at 15 GHz as measured with the Ryle telescope, the compactness ratio,  $\ell_h/\ell_s$  and the bolometric flux of the accretion disk as obtained from the *eqpair* models, and the 2–10 keV *RXTE*-ASM light curve, rebinned to a resolution of 5.6 d to smooth out the orbital variability. Error bars are not shown for clarity.

$F_{\text{disk}}$  computed from Eq. 3 to  $\sim 5 \cdot 10^{-9} \text{ erg cm}^{-2} \text{ s}^{-1}$ . We note that evolution of the soft excess obtained from the *compTT* fits is very similar to that from the *eqpair* fits, although in general *compTT* gives a disk flux that is  $\sim 70\%$  of that found with *eqpair*.

The hard spectral component is characterized by the compactness ratio,  $\ell_h/\ell_s$  and the optical depth  $\tau$  of the Comptonizing medium. Large  $\ell_h/\ell_s$  correspond to the hard state. As shown in Fig. 9,  $\tau$  increases with  $\ell_h/\ell_s$ , indicating the increased importance of the Comptonizing medium for higher  $\ell_h/\ell_s$ . Consequently, low  $\ell_h/\ell_s$  correspond to the soft state, such that there is an anticorrelation between  $\ell_h/\ell_s$  and the accretion disk luminosity (Fig. 10). This anticorrelation can be expressed as a power law dependence of the bolometric accretion disk luminosity,  $L_{\text{disk}}$ , and  $\ell_h/\ell_s$ ,

$$L_{\text{disk}} \propto (\ell_h/\ell_s)^{-0.19} \quad (4)$$

This relationship holds over the  $\sim 1$  order of magnitude in variation of the disk luminosity. Our fits thus indicate very smooth relationships between the parameters of the Comptonizing medium and the accretion disk, with no jumps being present that would indicate that the source behavior suddenly changes when the source switches its state. This behavior is also clearly seen in Fig. 11, where we show how the *eqpair* parameters relate to the continuum shape as described by the broken power law models. For large values of  $\ell_h/\ell_s$ , the photon index saturates at  $\sim 1.6$  and the folding energy approaches its canonical value of  $\gtrsim 150 \text{ keV}$ . Not unexpectedly, for lower  $\ell_h/\ell_s$  as the soft state is approached,  $\Gamma_2$  softens and  $E_{\text{fold}}$  decreases, resulting in a more curved hard X-ray spectrum.

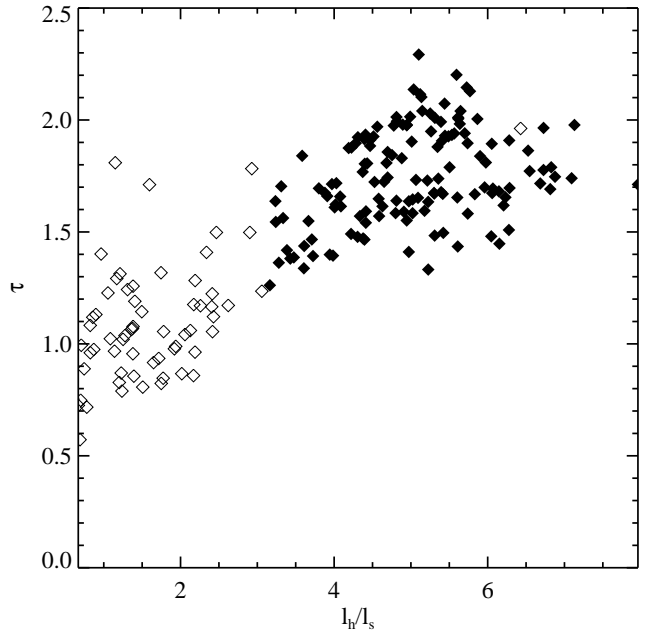


**Fig. 9.** Relationship between the compactness ratio of the Comptonizing medium,  $\ell_h/\ell_s$ , and the optical depth  $\tau$  of the Comptonizing medium for the *eqpair* models. Symbols are the same as in Fig. 3.

We now briefly turn to the evolution of the bolometric flux of Cyg X-1. Based on *RXTE* and *CGRO* data, Zhang et al. (1997) claimed that the difference in bolometric luminosity of

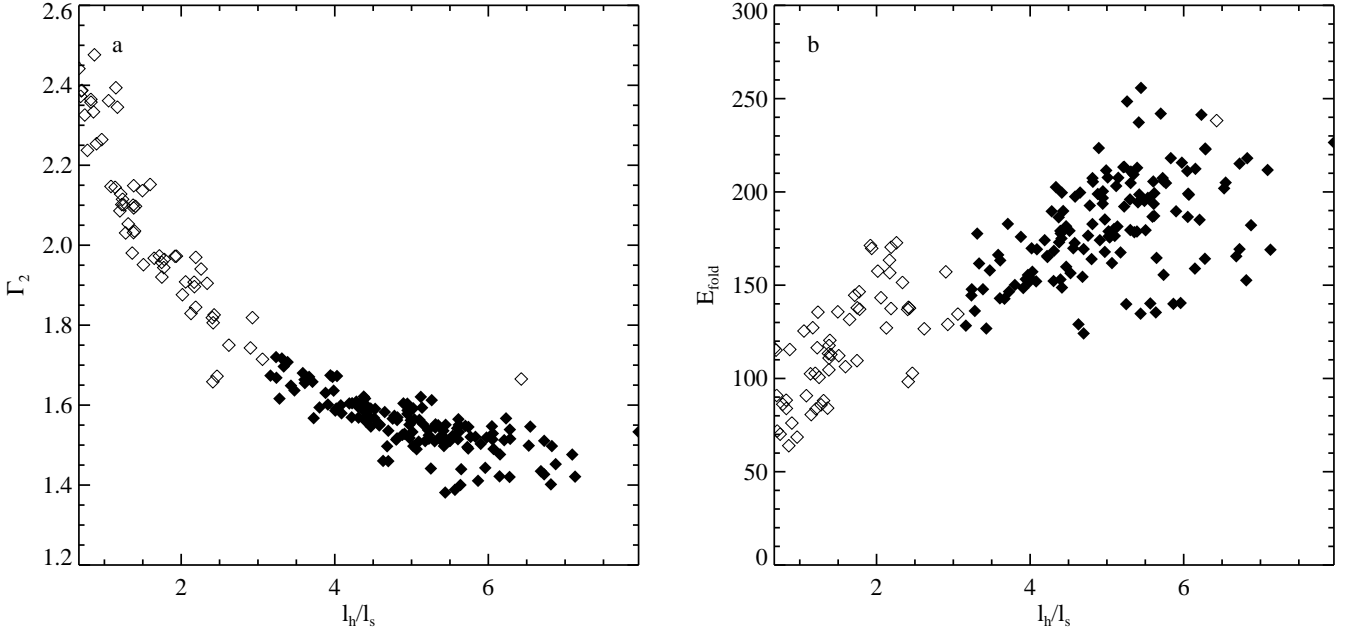


**Fig. 11.** Relationship between  $\ell_h/\ell_s$  and the shape of the X-ray spectrum above 10 keV as found from the broken power law fits. **a)** Correlation between  $\ell_h/\ell_s$  and the photon index,  $\Gamma_2$ , **b)** Correlation between  $\ell_h/\ell_s$  and the folding energy,  $E_{\text{fold}}$ .

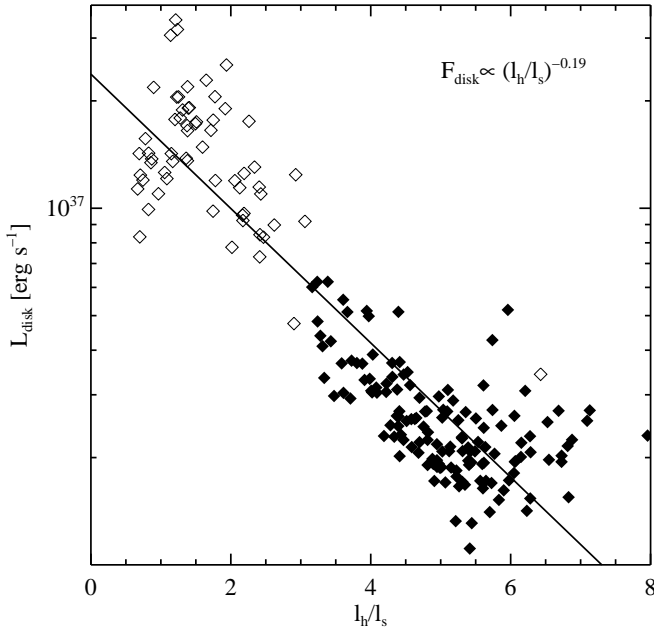


**Fig. 10.** The bolometric luminosity of the accretion disk,  $L_{\text{disk}}$ , computed assuming a distance of  $d = 2$  kpc, shows a power law dependence on the compactness ratio of the Comptonizing medium,  $\ell_h/\ell_s$ . Symbols used are identical to Fig. 3.

Cyg X-1 between the 1996 hard and soft states was  $\lesssim 50\%$ – $70\%$ , a statement later revisited by Zdziarski et al. (2002). Based on a small number of observations, these authors found that the bolometric flux of the source was higher by a factor of 3–4 in the soft state. The availability of our broad band fits allows us to confirm Zdziarski et al. (2002)’s earlier re-

sults: During the *RXTE* campaign, the mean bolometric unabsorbed flux of Cyg X-1 was  $4.3 \cdot 10^{-8} \text{ erg cm}^{-2} \text{ s}^{-1}$ , with a minimum flux of  $2.4 \cdot 10^{-8} \text{ erg cm}^{-2} \text{ s}^{-1}$  measured on 2003 January 10 (observation P60090/23.14off), and a maximum flux of  $9.1 \cdot 10^{-8} \text{ erg cm}^{-2} \text{ s}^{-1}$  measured on 2002 March 25 (observation P60090/02.14off). Assuming a distance of 2 kpc, these values correspond to a mean source luminosity of  $2.1 \cdot 10^{37} \text{ erg s}^{-1}$ , varying between  $1.2 \cdot 10^{37} \text{ erg s}^{-1}$  and  $4.4 \cdot 10^{37} \text{ erg s}^{-1}$ . These luminosity values are extremes; in general we find the luminosity of Cyg X-1 during the soft states to be approximately twice that of the hard state phases. Cyg X-1 thus has a long-term average luminosity of  $(0.01\text{--}0.02) L_{\text{Edd}}$ , assuming a black hole mass between 10 and 15 solar masses (Ziółkowski 2005; Herrero et al. 1995). Fig. 12 shows unfolded spectra for two of the more extreme observations of Cyg X-1, illustrating the strong spectral variability of the source.

Finally, we discuss the variability of the reprocessing features, i.e., the covering factor of the reflecting medium,  $\Omega/2\pi$ , and the Fe K $\alpha$  line. Fig. 13 shows that  $\Omega/2\pi \sim 0.15$  for  $\ell_h/\ell_s \gtrsim 4$ , indicating moderate amounts of reflection during the hard state. There is a moderate trend for  $\Omega/2\pi$  to decrease with increasing  $\ell_h/\ell_s$  (and increasing  $\tau$ ), although this trend is somewhat weaker and less distinct than previously claimed anti-correlations between reflection fraction and spectral hardness (Zdziarski et al. 2003; Zdziarski et al. 1999, and references therein). For our observations, the *eqpair* and the *compTT* fits show a similar relative behavior; however,  $\Omega/2\pi$  derived from *eqpair* is larger by  $\sim 0.1$ . This slightly larger fitted covering factor is likely due to the usage of a relativistic smeared reflection continuum in the *eqpair* fits; reflection in the *compTT* model is artificially reduced to minimize the sharp Fe edge in the reflection model used with those latter fits. There may also be influences from the different shapes of the expo-

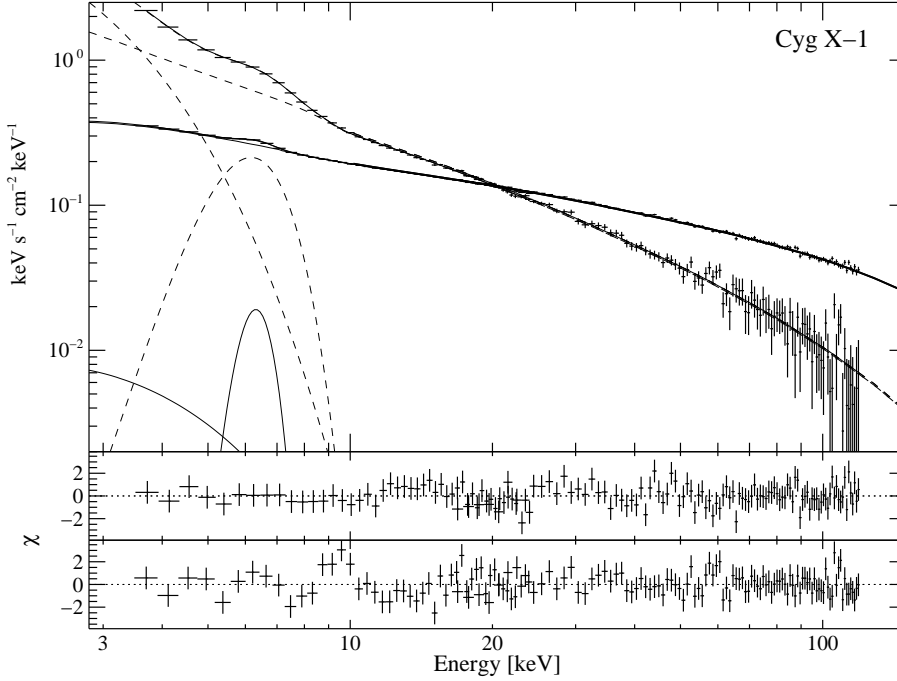


**Fig. 12.** Unfolded spectra and residuals for the eqpair fits of the Cyg X-1 observations of 2003 January 10 (P60090/23.14off; hard spectrum) and 2003 July 29 (P60090/35.14off; soft spectrum), illustrating the typical spectral variability of the source.

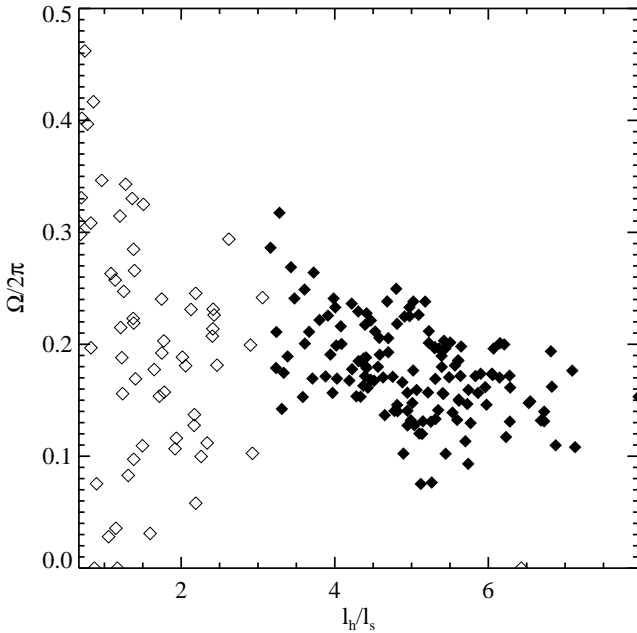


**Fig. 13.** Correlation between the compactness ratio of the Comptonizing medium,  $\ell_h/\ell_s$ , and the covering factor of the reflector,  $\Omega/2\pi$ . Symbols are the same as in Fig. 3.

nential cutoff in these two models. In the eqpair models, as the source approaches the soft state and  $\ell_h/\ell_s$  decreases, there is no clear correlation with  $\Omega/2\pi$ . The reflection fraction varies in a seemingly independent manner, although in general our highest fitted reflection fractions come from the soft state. Again this is reminiscent of the behavior already seen in the compTT fits (Fig. 7).

The second indicator for reprocessing in cold material, the Fe  $K\alpha$  line, does not show a correlated behavior with any of

the spectral parameters considered here. This lack of correlation is puzzling. Since the Fe  $K\alpha$  line is thought to be the result of fluorescence in the accretion disk, we would expect the Fe line to track  $\Omega/2\pi$ , i.e., the variation of the Compton reflection component. Similar to our fits with the broken power law or the compTT model, there is a larger fraction of fits in which the Fe  $K\alpha$  line has an energy that is significantly below 6.4 keV. The residuals for these observations often show the Xe L edge calibration feature, indicating that calibration effects might lead at least in part of the observations to spurious Fe  $K\alpha$  line parameters, although we cannot exclude other effects, such as a more complex shape of the soft excess. As already indicated above, however, neither the addition of a Compton component (Gierliński et al. 1999) nor the substitution of the diskbb soft component by a diskpnp component result in a better description of the soft excess and the Fe  $K\alpha$  line.

### 3.6. Disk–Jet Interaction

As we have seen in Fig. 8, in agreement with studies of other sources, we find evidence for correlated radio and X-ray variability. Due to the comparably low luminosity variation of a factor of  $\sim 4$ , Cyg X-1 is not an ideal source to study disk-jet correlations across widely separated states, as occur in X-ray transients that show factors of 100 to 1000 luminosity changes (Fender & Belloni 2004; Fender et al. 2004). The proximity of Cyg X-1 to the threshold between the hard and soft states, however, allows us to study this crucial transition interval in much greater detail than for transients.

To parameterize our data with the least possible theoretical bias, we can use the results from the broken power law fits. As shown in Sect. 3.3, these fits indicate the presence of two spectral components that vary in a correlated manner as described by the  $\Gamma_1$ – $\Gamma_2$  correlation. We show in Fig. 14 that

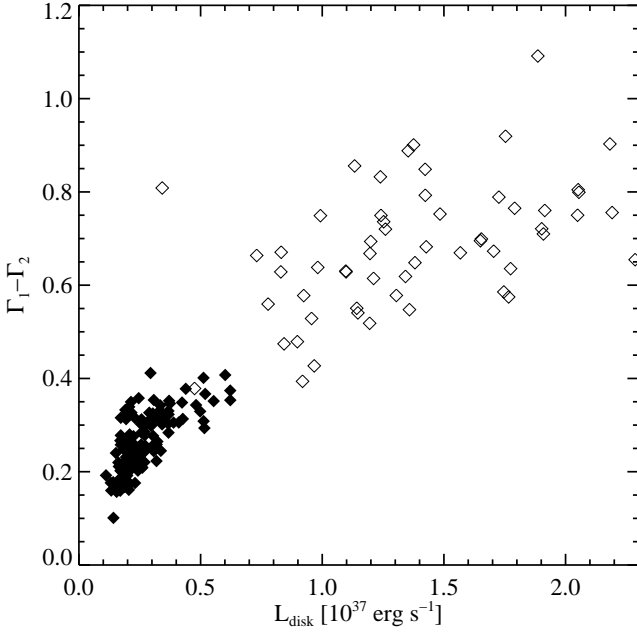


**Fig. 14.** The power law break,  $\Delta\Gamma$ , of the broken power law fits can be interpreted as a measure of the bolometric accretion disk luminosity.

there is an almost linear relation between the soft excess luminosity found from Comptonization fits and  $\Delta\Gamma = \Gamma_1 - \Gamma_2$ . In Comptonization models, therefore, one can interpret the power law break in part as a measure of the bolometric accretion disk luminosity, although part of the break can also be caused by the  $\Omega$ - $\Gamma$ -relationship.

Alternatively, however, in models explaining the X-ray spectra of BHC in terms of emission from along a jet, the power law break describes the transition from synchrotron radiation (as well as accretion disk emission) to a synchrotron self-Compton spectrum that is modified by Compton reflection (Markoff et al. 2003, 2005; Markoff & Nowak 2004; Nowak et al. 2005). Figure 15 provides an important benchmark for such models. For  $\Delta\Gamma \lesssim 0.5$ , i.e., most hard state observations, the radio flux is seemingly independent of  $\Delta\Gamma$ , while above that threshold strong variations of the radio flux are observed.

Using the Comptonization interpretation of the X-ray spectrum, we can study how the radio emission and the Comptonizing medium interact. For such a study the *eqpair* models are especially interesting, since  $\ell_h/\ell_s$  is a measure of the energetics of the Comptonizing medium. We find that the radio flux is highest at intermediate  $\ell_h/\ell_s$  ( $\ell_h/\ell_s \sim 3$ ; Fig. 16). This behavior is a consequence of the “failed state transitions”, where Cyg X-1 shows characteristic flaring behavior in the radio, similar to what has also been seen in GX 339-4 and other jet sources (Corbel et al. 2000, 2003; Hannikainen et al. 1998; Fender et al. 2004, see also Figs. 1 and 8). Note that  $\ell_h/\ell_s = 3$  corresponds to a soft photon index of  $\Gamma_1 \sim 2.1$ , consistent with the upper limit for the hard state  $\Gamma_1$  as defined by Remillard (2005). Note also that there seems to be a much tighter rela-

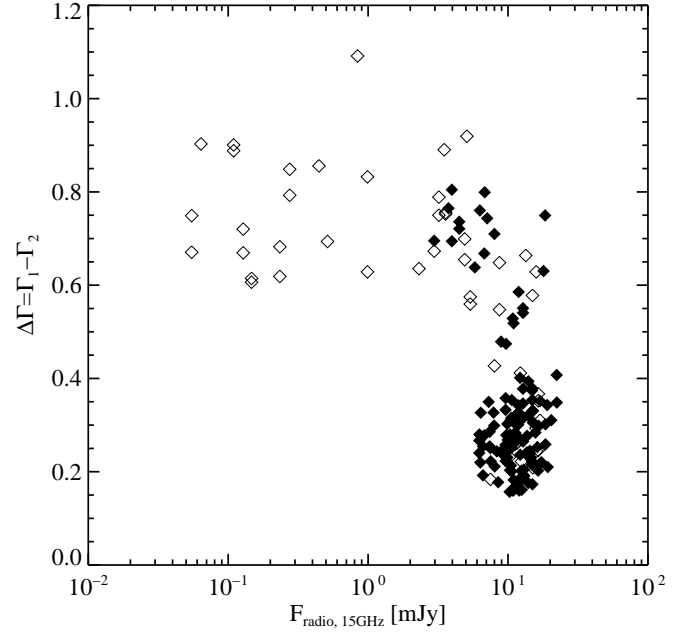


**Fig. 15.** For power law breaks  $\lesssim 0.5$  the radio flux varies seemingly independent of the X-ray color, expressed here as the ratio between the 2–10 keV and the 10–50 keV flux. Symbols used are identical to Fig. 3. See text for further explanation.

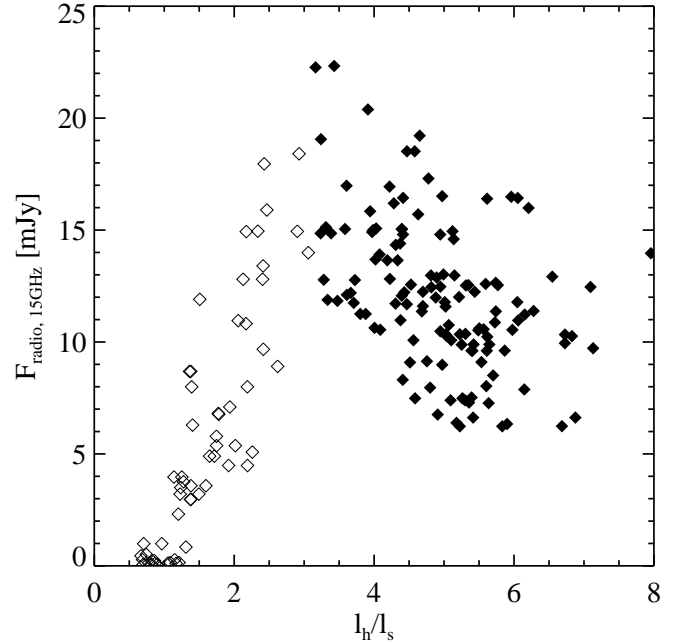


**Fig. 16.** Correlation between the 15 GHz radio flux and the compactness ratio of the Comptonizing medium,  $\ell_h/\ell_s$ . The increase in radio flux for intermediate values of  $\ell_h/\ell_s$  is due to the radio flares usually associated with “failed state transitions” and the intermediate state. The radio flux shown is the mean radio flux averaged over the 5.6 d orbital timescale surrounding each *RXTE* measurement. Symbols used are the same as in Fig. 3.

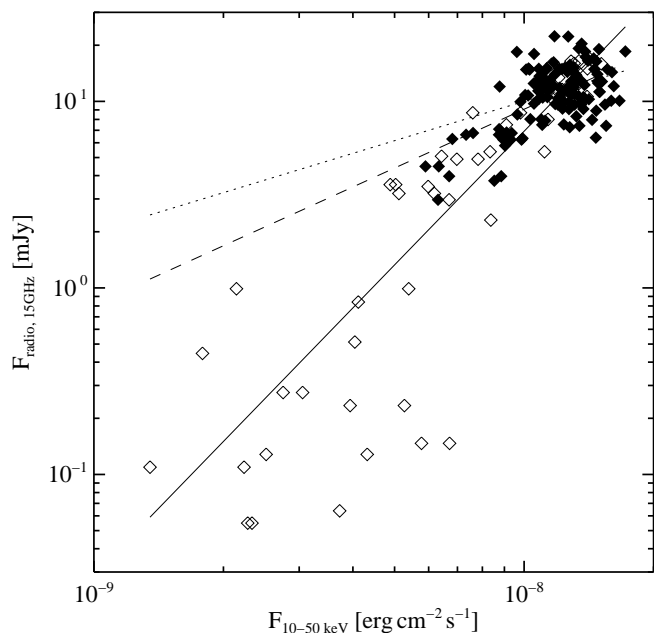


**Fig. 17.** Correlation between the 10–50 keV hard X-ray flux and the 15 GHz radio flux. The dotted line corresponds to the canonical  $F_R \propto F_X^{0.7}$  relation (Corbel et al. 2003; Gallo et al. 2003), the dashed line is  $F_R \propto F_X^{1.05}$  determined from the hard state data, the solid line is  $F_R \propto F_X^{2.38}$  found from all Cyg X-1 measurements.

tionship between the radio flux and  $\ell_h/\ell_s$  for the soft state compared to the scatter seen for the hard state.

In general, BHC for which radio fluxes have been measured exhibit a strong correlation between the radio and the X-ray flux (Gallo et al. 2003; Merloni et al. 2003). For Cyg X-1, this correlation becomes less well pronounced as the soft X-ray flux increases (paper iii; Gallo et al. 2003). We likewise do not find a significant relationship between the radio flux and either the bolometric flux or the disk emission. As already described in paper iii and by Nowak et al. (2005), however, the radio flux correlates well with the 10–50 keV hard X-ray flux ( $\rho = 0.625$ ). For 15 GHz fluxes above 0.1 mJy, the lowest flux at which the source was detected during the campaign, we find that the 10–50 keV X-ray flux,  $F_{10-50}$ , can be found from

$$\log_{10} \frac{F_{10-50}}{\text{erg cm}^2 \text{ s}^{-1}} = -8.27 + 0.320 \log_{10} \frac{F_{15\text{GHz}}}{\text{mJy}} \quad (5)$$

with an uncertainty of less than 15%. Here, the radio flux is again the mean flux determined over one orbital period of the system to average out the orbital variability (Brocksopp et al. 1999a).

This result is in strong support of the idea that the hard X-ray flux is tightly coupled to the radio, suggesting a possible physical connection between the regions in which this radiation is produced. Note that for many X-ray transients the radio–X-ray relationship is found from the 2–10 keV *RXTE*-ASM data, which is possible only because of the less complex soft excess in these Roche lobe accreting systems. Overall, however, the radio behavior of Cyg X-1 as expressed by Eq. 5 seems

to be slightly different from that of X-ray transients, where Gallo et al. (2003) and Corbel et al. (2003) find that the radio flux,  $F_R$ , and X-ray flux,  $F_X$  are related by  $F_R \propto F_X^{0.7}$ . Such a scaling is expected in various models in which the X-ray and radio producing regions are connected, either by the X-rays originating in a jet (Falcke & Biermann 1996; Corbel et al. 2003; Markoff et al. 2003, 2005) or by the X-rays originating in an advection dominated type of accretion flow that is coupled to the radio outflow (Heinz & Sunyaev 2003). Fig. 17 shows that for Cyg X-1 there are indications that the radio–X-ray relationship is steeper than this canonical value. Taking all observations with available radio fluxes into account, we find  $F_R \propto F_X^{2.38}$  (Fig. 17, solid line). Limiting ourselves to the hard state observations only, where the radio fluxes are best determined, we find  $F_R \propto F_X^{1.05}$  (Fig. 17, dashed line), which, given the uncertainty of the flux determination, can be considered as consistent with the  $F_R \propto F_X^{0.7}$  relationship. Similarly steep radio–X-ray relationships have been seen in the black hole candidate XTE J1908+094 (Jonker et al. 2004) and in the neutron star system 4U 1728–34 (Migliari et al. 2003).

## 4. Summary

In this paper we have analyzed  $\sim 200$  observations of Cygnus X-1 in all of its states. The spectral parameters are in qualitative agreement with those found for Comptonization models of earlier observations (e.g., Pottschmidt et al. 2003a; Di Salvo et al. 2001; Frontera et al. 2001; Gilfanov et al. 1999; Gierliński et al. 1999; Dove et al. 1998). The availability of the large number of observations allows us to study the variation of the spectral parameters in this black hole candidate in unprecedented detail. This has revealed a large number of interesting correlations that must be explained by models for the emission process and emission geometry of Cyg X-1. In summary, the main results of the spectral analysis are as follows:

1. Cyg X-1 changed its behavior in early 2000. While it was predominantly a hard state source before that, since 2000 the source spent  $\sim 34\%$  of the time in the intermediate and the soft state (see also paper i). The physical reason for this change in behavior could be related to changes in the mass loss rate from HDE 226868.
2. The spectral continuum of Cyg X-1 is very simple and can be well described at the level of the *RXTE* resolution by a broken power law with an exponential cutoff.
3. More physical models such as the two Comptonization models considered here try to reproduce this simplicity and, for the hard state, result in  $\chi^2$  values comparable (but slightly worse) than the broken power law fits.
4. At the  $\chi^2$  level, simple and advanced Comptonization models cannot be distinguished and the qualitative variation of their parameters is similar. From our modeling, a purely thermal electron distribution seems to be sufficient to describe the spectra in the hard and soft state observations, at least in the  $\sim 3$ –120 keV energy range considered here.
5. There is a continuum of spectra between the hard state and the soft state, with no strong discontinuities found in the behavior of the spectral parameters. This continuous vari-

ation is in strong contrast with the changes in timing behavior, where the states are clearly distinguishable. For example, the intermediate state and failed state transitions have increased X-ray time lags (Pottschmidt et al. 2000) and changed power spectra (paper I).

6. This continuous distribution of parameters from the soft to the hard state leads to robust correlations between spectral parameters, reflecting trends in the continuum of spectral shapes of Cyg X-1. For the broken power law fits, the most important correlation is that between the soft and the hard power law index, for the Comptonization fits there is a power law relationship between the soft excess luminosity and the compactness ratio,  $L_{\text{disk}} \propto (\ell_h/\ell_s)^{-0.19}$ .
7. For the compTT models, the Comptonizing plasma shows a steady behavior during the hard state and strongly varies during the soft state (with a similar behavior in the reflection covering factor,  $\Omega/2\pi$ ). During the hard state, the soft excess properties vary seemingly independently from the Comptonizing plasma.
8. Although both Comptonization models show a slight anti-correlation between spectral hardening and reflection fraction,  $\Omega/2\pi$ , it is not as pronounced as has been previously claimed (Zdziarski et al. 2003, and references therein). It is likely that part of this correlation is in fact related to correlations between broad-band soft and hard continuum components.
9. The Fe K $\alpha$  line is found to be only moderately broad in the broken power law fits, consistent with earlier results (Frontera et al. 2001; Gilfanov et al. 1999). An increased broadening seen in the Comptonization models is likely not a physical effect but rather is caused by an attempt of the fits to improve the modeling of the soft excess component.
10. For the hard state, Cyg X-1 follows the general radio–X-ray relation,  $F_R \propto F_X^{0.7}$ , although there are indications that the relationship is slightly steeper when also taking the soft state data into account.

A further interpretation of these results in terms of physical models requires the consideration of the simultaneous variation of the timing parameters, which we will present in a further paper in this series.

**Acknowledgements.** We thank Thomas Gleißner, Sara Benlloch, and William “Biff” Heindl for many discussions and help with the data screening and extraction during the years it took to assemble the data from the Cyg X-1 campaign and the anonymous referee for his/her comments. This work has been partly funded by NASA contract NAS5-30720, NASA grant SV3-73016, by Deutsches Zentrum für Luft- und Raumfahrt grant 50 OR 302 and by travel funds from the Deutscher Akademischer Austauschdienst and the National Science Foundation (NSF contract INT-0233441). The Ryle telescope is supported by PPARC. This work has made use of data obtained from the High Energy Astrophysics Science Archive Research Center (HEASARC), provided by NASA’s Goddard Space Flight Center. The Green Bank Interferometer was a facility of the National Science Foundation operated by the National Radio Astronomy Observatory in support of NASA High Energy Astrophysics programs. The University of Warwick Centre for Scientific Computing provided significant computing resources through its Cluster of Workstations

(COW). We thank the Aspen Center for Physics for its hospitality during the final stages of the preparation of this paper.

## References

- Arnaud, K. A. 1996, in *Astronomical Data Analysis Software and Systems V*, ed. J. H. Jacoby & J. Barnes, Astron. Soc. Pacific, Conf. Ser. No. 101 (San Francisco: Astron. Soc. Pacific), 17
- Axelsson, M., Borgonovo, L., & Larsson, S. 2005, *A&A*, 438, 999
- Bałucińska-Church, M., Belloni, T., Church, M. J., & Hasinger, G. 1995, *A&A*, 302, L5
- Balbus, S. A. & Hawley, J. F. 1998, *Rev. Mod. Phys.*, 70, 1
- Bałucińska-Church, M., Church, M. J., Charles, P. A., et al. 2000, *MNRAS*, 311, 861
- Bałucińska-Church, M. & McCammon, D. 1992, *ApJ*, 400, 699
- Belloni, T. 2004, *Nucl. Phys. B (Proc. Suppl.)*, 132, 337
- Belloni, T., Homan, J., Casella, P., et al. 2005, *A&A*
- Beloborodov, A. M. 1999, *ApJ*, 510, L123
- Beloborodov, A. M. & Illarionov, A. F. 2001, *MNRAS*, 323, 167
- Bevington, P. R. & Robinson, D. K. 1992, *Data Reduction and Error Analysis for the Physical Sciences*, 2<sup>nd</sup> edn. (New York: McGraw-Hill)
- Bondi, H. & Hoyle, F. 1944, *MNRAS*, 104, 273
- Brocksopp, C., Fender, R. P., Larionov, V., et al. 1999a, *MNRAS*, 309, 1063
- Brocksopp, C., Tarasov, A. E., Lyuty, V. M., & Roche, P. 1999b, *A&A*, 343, 861
- Coppi, P. 1999, in *High Energy Processes in Accreting Black Holes*, ed. J. Poutanen & R. Svensson, Astron. Soc. Pacific, Conf. Ser. No. 161 (San Francisco: Astron. Soc. Pacific), 375
- Coppi, P. 2004, in *X-Ray Timing 2003: Rossi and Beyond*, ed. P. Kaaret, F. K. Lamb, & J. Swank, Am. Inst. Phys., Conf. Ser. No. 714 (Woodbury: AIP), 79–88
- Coppi, P. S. 1992, *MNRAS*, 258, 657
- Corbel, S., Fender, R., Tzioumis, T., et al. 2000, *A&A*, 359, 251
- Corbel, S., Nowak, M. A., Fender, R. P., Tzioumis, A. K., & Markoff, S. 2003, *A&A*, 400, 1007
- Cui, W., Heindl, W. A., Rothschild, R. E., et al. 1997, *ApJ*, 474, L57
- Davidson, K. & Ostriker, J. P. 1973, *ApJ*, 179, 585
- Di Salvo, T., Done, C., Życki, P. T., Burderi, L., & Robba, N. R. 2001, *ApJ*, 547, 1024
- Dove, J. B., Wilms, J., & Begelman, M. C. 1997a, *ApJ*, 487, 747
- Dove, J. B., Wilms, J., Maisack, M. G., & Begelman, M. C. 1997b, *ApJ*, 487, 759
- Dove, J. B., Wilms, J., Nowak, M. A., Vaughan, B., & Begelman, M. C. 1998, *MNRAS*, 289, 729
- Esin, A. A., Narayan, R., Cui, W., Grove, J. E., & Zhang, S.-N. 1998, *ApJ*, 505, 854
- Falcke, H. & Biermann, P. L. 1996, *A&A*, 308, 321
- Fender, R. & Belloni, T. 2004, *ARA&A*, 42, 317
- Fender, R., Corbel, S., Tzioumis, T., et al. 1999, *ApJ*, 519, L165



- Fender, R. P., Belloni, T. M., & Gallo, E. 2004, *MNRAS*, 355, 1105
- Frontera, F., Palazzi, E., Zdziarski, A. A., et al. 2001, *ApJ*, 546, 1027
- Gallo, E., Fender, R., Kaiser, C., et al. 2005, *Nat*, 436, 819
- Gallo, E., Fender, R. P., & Pooley, G. G. 2003, *MNRAS*, 344, 60
- Gierliński, M. & Zdziarski, A. A. 2003, *MNRAS*, 343, L84
- Gierliński, M., Zdziarski, A. A., Done, C., et al. 1997, *MNRAS*, 288, 958
- Gierliński, M., Zdziarski, A. A., Poutanen, J., et al. 1999, *MNRAS*, 309, 496
- Gies, D. R., Bolton, C. T., Thomson, J. R., et al. 2003, *ApJ*, 583, 424
- Gilfanov, M., Churazov, E., & Revnivtsev, M. 1999, *A&A*, 252, 182
- Gleissner, T., Wilms, J., Pooley, G. G., et al. 2004a, *A&A*, 425, 1061, (paper III)
- Gleissner, T., Wilms, J., Pottschmidt, K., et al. 2004b, *A&A*, 414, 1041, (paper II)
- Göğüş, E., Finger, M. H., Kouveliotou, C., et al. 2004, *ApJ*, 609, 977
- Grove, J. E., Johnson, W. N., Kroeger, R. A., et al. 1998, *ApJ*, 500, 899
- Haardt, F. & Maraschi, L. 1991, *ApJ*, 380, L51
- Haardt, F. & Maraschi, L. 1993, *ApJ*, 413, 507
- Haardt, F., Maraschi, L., & Ghisellini, G. 1997, *ApJ*, 476, 620
- Hannikainen, D. C., Hunstead, R. W., Campbell-Wilson, D., & Sood, R. K. 1998, *A&A*, 337, 460
- Hatchett, S. & McCray, R. 1977, *ApJ*, 211, 552
- Heinz, S. & Sunyaev, R. A. 2003, *MNRAS*, 343, L59
- Herrero, A., Kudritzki, R. P., Gabler, R., Vilchez, J. M., & Gabler, A. 1995, *A&A*, 297, 556
- Homan, J., Buxton, M., Markoff, S., et al. 2005, *ApJ*, 624, 295
- Homan, J., Wijnands, R., van der Klis, M., et al. 2001, *ApJS*, 132, 377
- Ibragimov, A., Poutanen, J., Gilfanov, M., Zdziarski, A. A., & Shrader, C. R. 2005, *MNRAS*, 362, 1435
- Jahoda, K., Markwardt, C. B., Radeva, Y., et al. 2005, *ApJS*, submitted (available at <http://lhea-www.gsfc.nasa.gov/docs/xray/xte/pca/>)
- Jahoda, K., Swank, J. H., Giles, A. B., et al. 1997, in *EUV, X-Ray, and Gamma-Ray Instrumentation for Astronomy VII*, ed. O. H. Siegmund, Proc. SPIE No. 2808 (Bellingham, WA: SPIE), 59–70
- Jester, S. 2005, *ApJ*, 625, 667
- Jonker, P. G., Gallo, E., Dhawan, V., et al. 2004, *MNRAS*, 351, 1359
- Kalemci, E., Tomsick, J. A., Buxton, M. M., et al. 2005, *ApJ*, 622, 508
- Kalemci, E., Tomsick, J. A., Rothschild, R. E., et al. 2003, *ApJ*, 586, 419
- Kalemci, E., Tomsick, J. A., Rothschild, R. E., Pottschmidt, K., & Kaaret, P. 2001, *ApJ*, 563, 239
- Kong, A. K. H., Charles, P. A., Kuulkers, E., & Kitamoto, S. 2002, *MNRAS*, 329, 588
- Lampton, M., Margon, B., & Bowyer, S. 1976, *ApJ*, 208, 177
- Levine, A. M., Bradt, H., Cui, W., et al. 1996, *ApJ*, 469, L33
- Lightman, A. P. & Rybicki, G. B. 1979, *ApJ*, 229, L15
- Lightman, A. P. & White, T. R. 1988, *ApJ*, 335, 57
- Maccarone, T. J. & Coppi, P. S. 2003, *MNRAS*, 338, 189
- Magdziarz, P. & Zdziarski, A. A. 1995, *MNRAS*, 273, 837
- Makishima, K., Maejima, Y., Mitsuda, K., et al. 1986, *ApJ*, 308, 635
- Malzac, J., Beloborodov, A. M., & Poutanen, J. 2001, *MNRAS*, 326, 417
- Markoff, S., Nowak, M., Corbel, S., Fender, R., & Falcke, H. 2003, *A&A*, 397, 645
- Markoff, S. & Nowak, M. A. 2004, *ApJ*, 609, 972
- Markoff, S., Nowak, M. A., & Wilms, J. 2005, *ApJ*, in press (astro-ph/0509028)
- McClintock, J. & Remillard, R. A. 2003, in *Compact Stellar X-ray Sources*, ed. W. H. G. Lewin & M. van der Klis (Cambridge: Cambridge Univ. Press), in press (astro-ph/0306213)
- McConnell, M. L., Ryan, J. M., Collmar, W., et al. 2000, *ApJ*, 543, 928
- McConnell, M. L., Zdziarski, A. A., Bennett, K., et al. 2002, *ApJ*, 572, 984
- McHardy, I. M., Gunn, K. F., Uttley, P., & Goad, M. R. 2005, *MNRAS*, 359, 1469
- Meier, D. L. 2001, *ApJ*, 548, L9
- Merloni, A. & Fabian, A. C. 2002, *MNRAS*, 332, 165
- Merloni, A., Heinz, S., & di Matteo, T. 2003, *MNRAS*, 345, 1057
- Migliari, S., Fender, R. P., Rupen, M., et al. 2003, *MNRAS*, 342, L67
- Miller, J. M., Fabian, A. C., Wijnands, R., et al. 2002, *ApJ*, 578, 348
- Mitsuda, K., Inoue, H., Koyama, K., et al. 1984, *PASJ*, 36, 741
- Miyamoto, S., Kitamoto, S., Hayashida, K., & Egoshi, W. 1995, *ApJ*, 442, L13
- Nowak, M. A., Wilms, J., & Dove, J. B. 1999, *ApJ*, 517, 355
- Nowak, M. A. & Wilms, J. 1999, *ApJ*, 522, 476
- Nowak, M. A., Wilms, J., & Dove, J. B. 2002, *MNRAS*, 332, 856
- Nowak, M. A., Wilms, J., Heindl, W. A., et al. 2001, *MNRAS*, 320, 316
- Nowak, M. A., Wilms, J., Heinz, S., et al. 2005, *ApJ*, 626, 1006
- Pooley, G. G., Fender, R. P., & Brocksopp, C. 1999, *MNRAS*, 302, L1
- Pottschmidt, K., Wilms, J., Chernyakova, M., et al. 2003a, *A&A*, 411, L383
- Pottschmidt, K., Wilms, J., Nowak, M. A., et al. 2000, *A&A*, 357, L17
- Pottschmidt, K., Wilms, J., Nowak, M. A., et al. 2003b, *A&A*, 407, 1039, (paper I)
- Poutanen, J. & Fabian, A. C. 1999, *MNRAS*, 306, L31
- Puls, J., Kudritzki, R.-P., Herrero, A., et al. 1996, *A&A*, 305, 171
- Remillard, R. A. 2005, in *Texas@Stanford 2004*, ed. P. Chen, SLAC Electronic Conference Proceedings Archive, astro-ph/0504129
- Rothschild, R. E., Blanco, P. R., Gruber, D. E., et al. 1998, *ApJ*, 496, 538
- Shakura, N. I. & Sunyaev, R. 1973, *A&A*, 24, 337

- Shapiro, S. L., Lightman, A. P., & Eardley, D. 1976, *ApJ*, 204
- Sobczak, G. J., McClintock, J. E., Remillard, R. A., et al. 2000, *ApJ*, 544, 933
- Stern, B. E., Poutanen, J., Svensson, R., Sikora, M., & Begelman, M. C. 1995, *ApJ*, L13
- Stirling, A. M., Spencer, R. E., de la Force, C. J., et al. 2001, *MNRAS*, 327, 1273
- Sunyaev, R. A. & Trümper, J. 1979, *Nat*, 279, 506
- Tarasov, A. E., Brocksopp, C., & Lyuty, V. M. 2003, *A&A*, 402, 237
- Thorne, K. S. & Price, R. H. 1975, *ApJ*, 195, L101
- Tigelaar, S. P., Fender, R. P., Tilanus, R. P. J., Gallo, E., & Pooley, G. G. 2004, *MNRAS*
- Titarchuk, L. 1994, *ApJ*, 434, 570
- Titarchuk, L. & Hua, X.-M. 1995, *ApJ*, 452, 226
- Titarchuk, L. & Lyubarskij, Y. 1995, *ApJ*, 450, 876
- Tomsick, J. A. & Kaaret, P. 2000, *ApJ*, 537, 448
- Toor, A. & Seward, F. D. 1974, *AJ*, 79, 995
- Uttley, P., McHardy, I. M., & Papadakis, I. E. 2002, *MNRAS*, 332, 231
- Uttley, P., McHardy, I. M., & Vaughan, S. 2005, *MNRAS*, 359, 345
- Voloshina, I. B., Lyutyi, V. M., & Tarasov, A. E. 1997, *Astron. Lett.*, 23, 293
- Weisskopf, M. C., O'Dell, S. L., Paerels, F., et al. 2004, *ApJ*, 601, 1050
- Wen, L., Cui, W., Levine, A. M., & Bradt, H. V. 1999, *ApJ*, 525, 958
- Wilms, J., Allen, A., & McCray, R. 2000, *ApJ*, 542, 914
- Wilms, J., Nowak, M. A., Dove, J. B., Fender, R. P., & di Matteo, T. 1999, *ApJ*, 522, 460
- Wilms, J., Nowak, M. A., Pottschmidt, K., et al. 2001, *MNRAS*, 320, 327
- Zdziarski, A. A., Lubiński, P., Gilfanov, M., & Revnivtsev, M. 2003, *MNRAS*, 342, 355
- Zdziarski, A. A., Lubiński, P., & Smith, D. A. 1999, *MNRAS*, 303, L11
- Zdziarski, A. A., Poutanen, J., Paciesas, W. S., & Wen, L. 2002, *ApJ*, 578, 357
- Zhang, S. N., Cui, W., Harmon, B. A., et al. 1997, *ApJ*, 477, L95
- Ziōłkowski, J. 2005, *MNRAS*, 358, 851

## Appendix A: Revisiting the *RXTE* spectral calibration

In this Appendix we summarize our results for the spectral calibration of the *RXTE* based on HEASOFT 5.3.1. As shown, e.g., by Wilms et al. (1999), earlier HEASOFT versions exhibited a significant difference in spectral slope of  $\sim 0.05$  between the PCA and HEXTE, with PCA spectra being consistently softer than spectra derived from HEXTE and other missions. For observations of black holes, such a difference is especially worrisome since the apparent hardening implied by the older calibration can mimic a Compton reflection component. In HEASOFT 5.3.1, this discrepancy is now much smaller and fits to *RXTE* observations of the Crab nebula and pulsar give

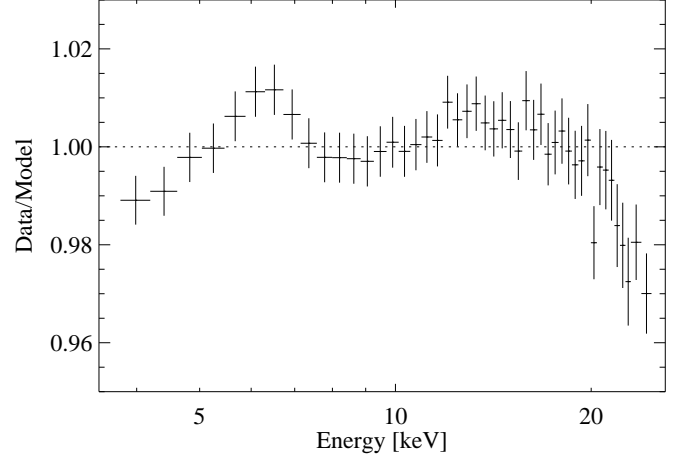


**Fig. A.1.** Ratio between data and the two power-law spectral model for the joint PCA-HEXTE fit of the *RXTE* observation of the Crab nebula and pulsar 40805-01-05-01 described in the text. For clarity, only the PCA residuals are shown. The error bars reflect the 0.5% systematics applied in our analysis.

the canonical spectral shape (see Jahoda et al. 2005, for an extensive discussion of the PCA calibration). For example, modeling the joint PCA and HEXTE data from *RXTE*'s Crab observation 40805-01-05-01 in 1999 we find that the joint spectrum can be described as the sum of two power laws with photon indices  $\Gamma_1 = 1.45$  and  $\Gamma_2 = 2.12$ . The nebula flux at 1 keV is found to be  $10.3 \text{ photons cm}^{-2} \text{ s}^{-1} \text{ keV}^{-1}$ , or about 8% higher than the canonical value of Toor & Seward (1974), the hard pulsar continuum contributes  $0.05 \text{ photons cm}^{-2} \text{ s}^{-1} \text{ keV}^{-1}$  at this energy (all values given are unabsorbed fluxes, absorption in the interstellar medium was taken into account by using the cross-sections and abundances of Wilms et al. 2000 and by assuming a H-equivalent column of  $N_H = 4.24 \times 10^{21} \text{ cm}^{-2}$  as found with *Chandra* by Weisskopf et al. 2004).

The ratio between the best fit Crab model (folded through the response matrix) and the data reveals the presence of energy dependent systematic uncertainties (Fig. A.1). These are strongest in the 4–6 keV band, around the Xe L-edge, where the deviation can amount to up to 1%, and above  $\sim 25$  keV. We chose to take these deviations into account by adding an energy independent uncertainty of 0.5% to the data. Applying this uncertainty to the Crab data gives a reduced chi-squared of  $\chi^2_{\text{red}} = 1.38$ . While a larger systematic uncertainty in the 4–6 keV band and above  $\sim 20$  keV would be justifiable in light of this result, we have decided not to include energy dependent systematics since experimenting showed that such systematics would affect the Fe  $K\alpha$  line region even more strongly than our current strategy (where the Fe  $K\alpha$  line energy is already biased towards energies below 6.4 keV). In addition, we only use PCA data from channels 6–52 of the standard2f data mode (approximately 3 keV–25 keV). For the HEXTE we use channels 17–117 (corresponding to  $\sim 18$  keV to  $\sim 120$  keV). The upper energy bound of 120 keV is set by the shorter observations in the sample and by the desire to have an uniform energy range for all observations. Note that HEXTE residuals in channels 17–20 typically show a linear increasing trend, which might be due to

calibration effects. We chose to include these channels anyway to increase the overlap between the PCA and HEXTE. When ignoring these HEXTE channels, the  $\chi^2$  of our fits typically decreases without significant changes of the best fit parameters.

In addition to the difference in spectral slope, earlier HEASOFT versions also showed a very significant overestimate of the PCA flux with respect to the HEXTE, with the PCA fluxes being consistently higher by  $\sim 30\%$ . This overestimate can be taken into account in  $\chi^2$ -fitting by multiplying the spectral model instrument dependent constant. Traditionally, this normalization constant was set to 1 for the PCA and let vary for the HEXTE. This traditional approach is unfortunate, since it implies that the flux normalization of the HEXTE is uncertain, while in reality it was the PCA that showed clear deviations in flux with respect to other instruments. For consistency with other studies, however, here we continue using the traditional approach. For all different spectral models used in this paper, we find that under HEASOFT 5.3.1 both instruments now agree remarkably well, with the distribution of the constant values being consistent with a normal distribution of mean 1.01 and standard deviation 0.03. We still chose to include the constant in our final fits, as in individual observations a mismatch between the PCA and the HEXTE is possible, for example for those observations where the PCA downtime becomes important<sup>4</sup>. There are only 7 observations with constants more than  $2\sigma$  away from the mean. Except for the significantly deviating normalization constant, these observations are not remarkable in any other way, and are therefore included in our further analysis, although the cause for the deviation is currently unknown. We conclude, therefore, that for the overwhelming majority of observations there is now agreement in the PCA and HEXTE derived fluxes.

## Appendix B: Confidence Intervals and *RXTE* Systematic Errors

As shown in the previous appendix, the high signal to noise observations from *RXTE* require us to take the systematic error of the instrument into account in order to obtain reasonable spectral parameters. In general, this is done by adding the systematic error in quadrature to the Poisson errors estimated from the observation. For instruments such as the PCA it can happen that the systematic error starts dominating the overall error. As a consequence, the standard “ $\chi^2_{\min} + \Delta\chi^2$ ”-procedure for obtaining confidence intervals, as outlined, e.g., by Lampton et al. (1976) or Bevington & Robinson (1992), does not apply since it is based on the assumption that the variance of the data points is due to a Gaussian distribution. Since the addition of systematic errors decreases the  $\chi^2$  sum, confidence intervals estimated using the Lampton et al. (1976) prescription in the presence of systematic errors are significantly larger than what is justified from statistical grounds.

**Table B.1.** Error bars for a representative observation of Cyg X-1, computed using the prescription of Lampton et al. (1976). See text for further explanation.

Parameter	value	90% error bar	
		with	without
		systematics	
$kT_{\text{in}}$ [keV]	0.855	(−0.02, +0.03)	(−0.01, +0.06)
$A_{\text{diskbb}}$	1276	(−175, +203)	(−24, +40)
$kT_{\text{e}}$ [keV]	108	(−31, +45)	(−20, +27)
$\tau$	0.26	(−0.14, +0.13)	(−0.12, +0.15)
$A_{\text{comptt}}$ [ $10^{-2}$ ]	1.86	(−1.0, +1.1)	(−0.5, +0.7)
$\Omega/2\pi$ [%]	17.9	(−1.8, +1.3)	(−1.1, +1.1)
$\sigma_{\text{Fe K}\alpha}$ [keV]	1.01	(−0.05, +0.04)	(−0.006, +0.012)
$A_{\text{Fe K}\alpha}$ [ $10^{-2}$ ]	5.34	(−0.4, +0.4)	(−0.07, +0.08)
$C_{\text{HEXTE}}$	0.999	(−0.004, +0.005)	(−0.003, +0.003)

To study the influence of the systematic error on the confidence intervals in our observations, we have used a Monte Carlo simulation: We first determined the best fit parameters for the *comptt* model of observation P60090/16 (2002.10.06:15) using the Lampton et al. (1976) approach, including systematic errors. We then used this best fit model to simulate how this observation would look like if the PCA and HEXTE calibration were perfectly known. These simulated spectra were then refit without applying a systematic error and new confidence intervals were determined. The resulting 90% confidence intervals for both fits are shown in Table B.1 (Error bars at the 68% level can be obtained from the 90% confidence intervals to a sufficiently high precision by assuming that the uncertainty can be approximated by a normal distribution). Depending on the parameter, the error bars are smaller by a factor of 2 to 5, showing that the confidence interval is completely dominated by the systematic error.

Since the systematic error will affect all observations of the Cyg X-1 *RXTE* campaign in a similar way and since the major interest is in determining *trends* in the evolution of spectral parameters, using the overestimation of the range of the confidence intervals determined from individual observations would lead to misleading results. It is better, therefore, to talk about an “ensemble average” in determining the errors and to take the scatter found in individual relationships between the fit parameters of Cyg X-1 in a similar state as an estimate their uncertainty. For this reason, we have decided to not show the misleading individual error bars in the figures in the main part of this paper, although they are available in the online data accompanying this paper (Tables 1–3).

<sup>4</sup> PCA spectra were not downtime corrected as the spectral shape is not influenced by the downtime correction and as good indicators for the PCA downtime are not available for the time since the failure of the Xe layer of PCU0, which also changed the downtime behavior of that PCU.